Phase-Engineered Weyl Semi-Metallic $Mo_xW_{1-x}Te_2$ Nanosheets as a Highly Efficient Electrocatalyst for Dye-Sensitized Solar Cells

Shemsia Mohammed Hudie, Chuan-Pei Lee, Roshan Jesus Mathew, Tzu-En Chien, Yi-June Huang, Han-Ting Chen, Kuo-Chuan Ho, Chi-Ang Tseng, and Yit-Tsong Chen*

The emerging Weyl semi-metals with robust topological surface states are very promising candidates to rationally develop new-generation electrocatalysts for dye-sensitized solar cells (DSSCs). In this study, a chemical vapor deposition (CVD) method to synthesize highly crystalline Weyl semi-metallic $Mo_xW_{1-x}Te_2$ nanocrystals, which are applied for the counter electrode (CE) of DSSCs for the first time, are employed. By controlling the temperature-dependent phase-engineered synthesis, the nanocrystal grown at 760°C exhibits the mixed phases of semiconducting T_d- & $2H$-$Mo_{0.32}W_{0.67}Te_{2.01}$ with charge carrier density of $(1.20 \pm 0.02) \times 10^{19}$ cm^{-3}; whereas, the nanocrystal synthesized at 820°C shows a single phase of semi-metallic T_d-$Mo_{0.29}W_{0.72}Te_{1.99}$ with much higher carrier density of $(1.59 \pm 0.04) \times 10^{20}$ cm^{-3}. In the cyclic voltammetry (CV) analysis over 200 cycles, the $Mo_xW_{1-x}Te_2$-based electrodes show better stability in the I^-/I_3^- electrolyte than a Pt electrode. In DSSC tests, a T_d-$Mo_{0.29}W_{0.72}Te_{1.99}$-decorated CE achieves the efficiency (η) of 8.85%, better than those CEs fabricated with T_d- & $2H$-$Mo_{0.32}W_{0.67}Te_{2.01}$ (7.81%) and sputtered Pt (8.01%). The electrochemical impedance spectra reveal that the T_d-$Mo_{0.29}W_{0.72}Te_{1.99}$ electrode possesses low charge-transfer resistance in electrocatalytic reactions. These exceptional properties make Weyl semi-metallic T_d-$Mo_xW_{1-x}Te_2$ a potential electrode material for a wide variety of electrocatalytic applications.

1. Introduction

Owing to their potential to replace the Pt catalyst in electrochemical cells, transition metal dichalcogenide (TMD)-based catalysts have received tremendous research attention in recent years.[1] TMDs with the composition of MX_2, containing transition metals (M = Mo or W) and chalcogens (X = S, Se, or Te), hold covalent bonds within a layer and van der Waals interactions along the layer-by-layer stacking.[2] To date, several semiconductive TMDs have been employed as electrocatalysts in the energy conversion systems, such as dye-sensitized solar cells (DSSC)[3–4] and hydrogen evolution reactions (HER).[5] In electrocatalytic reactions, the specific chalcogen ligands and grain boundaries of TMDs were regarded as the active sites (e.g., the bridging and terminal S_2^{2-} and the apical and unsaturated S^{2-} in MoS_2),[6–8] whose catalytic activities can be improved by utilizing surface engineering strategies to create artificial vacancies/defects on the basal plane of semicondoctor-based TMD catalysts.[1–9] However, the lack of sufficient electron transfer on TMD-based catalysts

S. M. Hudie, C.-A. Tseng, T.-E. Chien, Prof. Y.-T. Chen
Department of Chemistry
National Taiwan University
Taipei 10617, Taiwan
E-mail: ytcchem@ntu.edu.tw

Dr. C.-P. Lee
Department of Applied Physics and Chemistry
University of Taipei
Taipei 10048, Taiwan

S. M. Hudie, R. J. Mathew, T.-E. Chien, C.-A. Tseng, Prof. Y.-T. Chen
Institute of Atomic and Molecular Sciences
Academia Sinica
P.O. Box 23-166, Taipei 106, Taiwan

S. M. Hudie, R. J. Mathew
Nano Science and Technology Program
Taiwan International Graduate Program
Academia Sinica
Taipei 11529, Taiwan

Y.-J. Huang, H.-T. Chen, Prof. K.-C. Ho
Department of Chemical Engineering
National Taiwan University
Taipei 10617, Taiwan

R. J. Mathew
Department of Engineering and System Sciences
National Tsing-Hua University
Hsinchu 30013, Taiwan

The ORCID identification number(s) for the author(s) of this article can be found under https://doi.org/10.1002/solr.201800314.

due to their semiconducting nature has been the major bottleneck to achieve high electrocatalytic performance.[10] Consequently, searching for other candidates to create alternative catalytic routes is essential for the new-generation catalysts of better electrochemical efficiency.

Topological Weyl semi-metals (TWS) are a new class of promising catalysts in electrochemcial cells and have stimulated a research focus currently.[11–17] A basic feature of TWS characterizes the Weyl nodes of opposite chirality separated in the momentum space to form a surface-state curve, known as Fermi arc.[18] This unique phenomenon allows TWS carrying charges much faster than ordinary semiconductors; furthermore, this unique transport property of TWS gives rise to ultrahigh charge mobility, large mangetoresistance, and electrical superconductivity, enabling TWS to be an ideal material for future technological applications, such as magnetic storage,[19] quantum computation,[20] and spintronics aplications.[11–17] A recent report reveals the potential of employing TWS in catalysis,[21] where the key concept behind this catalysis mechanism arises from the topologically protected surface states of TWS to serve as an effective charge transport platform. These topological surface states provide an alternative catalytic mechanism, in contrast to the traditional approach of increasing active edge sites or vacancies.[21–22] In particular, the type-II TWS have an inverted band structure with broken inversion symmetry, leading to the existence of topological surface states, which are stable against defects, impurities, and other surface modifications.[15,24] Moreover, the lattice distortion with spontaneous surface charge density wave on the basal plane[10,25–27] could provide an additional advantage to allow a rapid charge exchange in electrochemical reactions, thus improving the catalytic activities.[10] Ultimately, resolving the surface contamination in a corrosive electrolytic solution is one of the major concerns in catalysis; propitiously, this issue can be effectively addressed by using TWS as a catalyst, because the topologically protected surface states are robust and stable against contamination.[21,23,28]

$Mo_xW_{1-x}Te_2$, the most attractive group-6 TMD-based Type-II TWS by theoretical prediction, contains tunable topological surface states and is more stable than other TWS of the binary compounds, such as WTe_2 and $MoTe_2$.[29] The strength of the topological surface states of $Mo_xW_{1-x}Te_2$ depends directly on the length of Fermi arc, which can be tuned at the Brillouin zone by doping Mo (from 2 to 40%) into the WTe_2 system.[18,30–32] $Mo_xW_{1-x}Te_2$ is a layered crystal, in which a single layer of W/Mo is sandwiched between two Te layers and stacked along the z-axis via van der Waals interactions[18,33–34] (**Figure 1**a). It is interesting to note that the crystal phases of $Mo_xW_{1-x}Te_2$ can vary from the semiconducting *2H* phase (hexagonal, the $P6_3/mmc$ space group) to the semi-metallic *1T'* phase (monoclinic, the $P2_1/m$ space group) or T_d phase (orthorhombic, Pmn_{21} space group), where each of the polymorphisms of $Mo_xW_{1-x}Te_2$ possesses distinctive properties due to the differences in intrinsic charge density and lattice symmetry.[21] For instance, a semi-metallic T_d-$Mo_xW_{1-x}Te_2$ with the lattice constants of a = 6.282 Å, b = 3.496 Å, and c = 14.07 Å is the most stable phase at room temperature and possesses broken inversion symmetry, which is a prerequisite to hold the type-II TWS surface states.[12,30–32] In contrast, while semi-metallic *1T'*-$Mo_xW_{1-x}Te_2$

can exist only at >900 °C, semiconducting *2H*-$Mo_xW_{1-x}Te_2$ is stable at ≤760 °C but lacks broken inversion symmetry.[35] These TWS $Mo_xW_{1-x}Te_2$ of polymorphic crystal phases provide versatile alternatives to investigate their electrocatalytic activities for developing new-generation catalytic counter electrodes (CE) of DSSC.

DSSC has been a research topic since the past decades because of its low cost, easy fabrication, and relatively high sunlight-to-electricity conversion efficiency.[36] In DSSC, a CE is one of the basic components, along with a TiO_2 photo-anode, photosensitizer dye, and the I^-/I_3^--based electrolyte, to determine the DSSC performance and completes the electric circuit by catalyzing the I^-/I_3^- redox couple at the CE/electrolyte interface. Traditionally, a sputtered platinum (Pt) was utilized as the electrocatalyst for the CE of DSSC; despite the high electrocatalytic activity toward the I^-/I_3^- redox reaction by Pt, the wide application of Pt has been hindered by its high cost, low abundance on the Earth's surface, and surface contamination in electrocatalysis.[37] Therefore, developing a novel electrocatalyst by using topologically protected $Mo_xW_{1-x}Te_2$ can not only prevents the surface contamination in the I^-/I_3^- medium, but also facilitates the rapid charge transfers in the redox reaction of I^-/I_3^- via the highly active topological surface of $Mo_xW_{1-x}Te_2$ to enhance the catalytic kinetics.

A high-quality bulk crystal of $Mo_xW_{1-x}Te_2$ can be synthesized with a chemical vapor transport (CVT) method[34]; however, the preparation of layered nanostructures from the CVT-grown crystal requires exfoliation processes,[38–39] rendering a low yield of the product and impeding the generation of large-area film-like nanocrystals.[29] Comparatively, chemical vapor deposition (CVD) is a facile bottom-up synthesis approach with the advantages of growing high-quality nanocrystals of large lateral sizes, controllable thickness, and high crystallinity on specific substrates.[29,40] However, the CVD synthesis of telluride-based few-layered nanocrystals, such as MTe_2 (M = Mo or W), remains challenging due to the very small difference in the electronegativities between Mo/W and Te (by ≈0.3–0.4 eV only) to form stable chemical bonds.[26] Notwithstanding the structural instability of binary MTe_2, the alloy system of $Mo_xW_{1-x}Te_2$ (x = 2–40%) is stable at room temperature and exhibits a tunable TWS surface state. Another unique feature of $Mo_xW_{1-x}Te_2$ is the existence of various crystal phases (including semiconductive *2H* and semi-metallic *1T'* and T_d), among which the energy differences are very small (<0.1 eV).[41] Therefore, it takes on challenges to synthesize the pure crystal phases of these polymorphic structures.[41] Consequently, developing a phase-engineered synthetic strategy to control the growth of $Mo_xW_{1-x}Te_2$ nanocrystals is essential for fundamental research and a wide range of practical electrocatalytic applications.

In this study, we conducted the temperature-based phase-engineered synthesis of highly crystalline $Mo_xW_{1-x}Te_2$ nanosheets on carbon cloth (CC) (denoted by $Mo_xW_{1-x}Te_2$/CC), for the first time, to serve as a CE of DSSC for electrocatalytic applications. We found that the growth temperature in the CVD reaction plays a key role to determine the phase and stoichiometry of the synthesized $Mo_xW_{1-x}Te_2$ nanocrystal. While a mixture of semiconductive (*2H*) and semi-metallic (T_d) phases of T_d- & *2H*-$Mo_{0.32}W_{0.67}Te_{2.01}$ nanocrystals were grown at 760 °C, only a single phase of T_d-$Mo_{0.29}W_{0.72}Te_{1.99}$ nanocrystals was
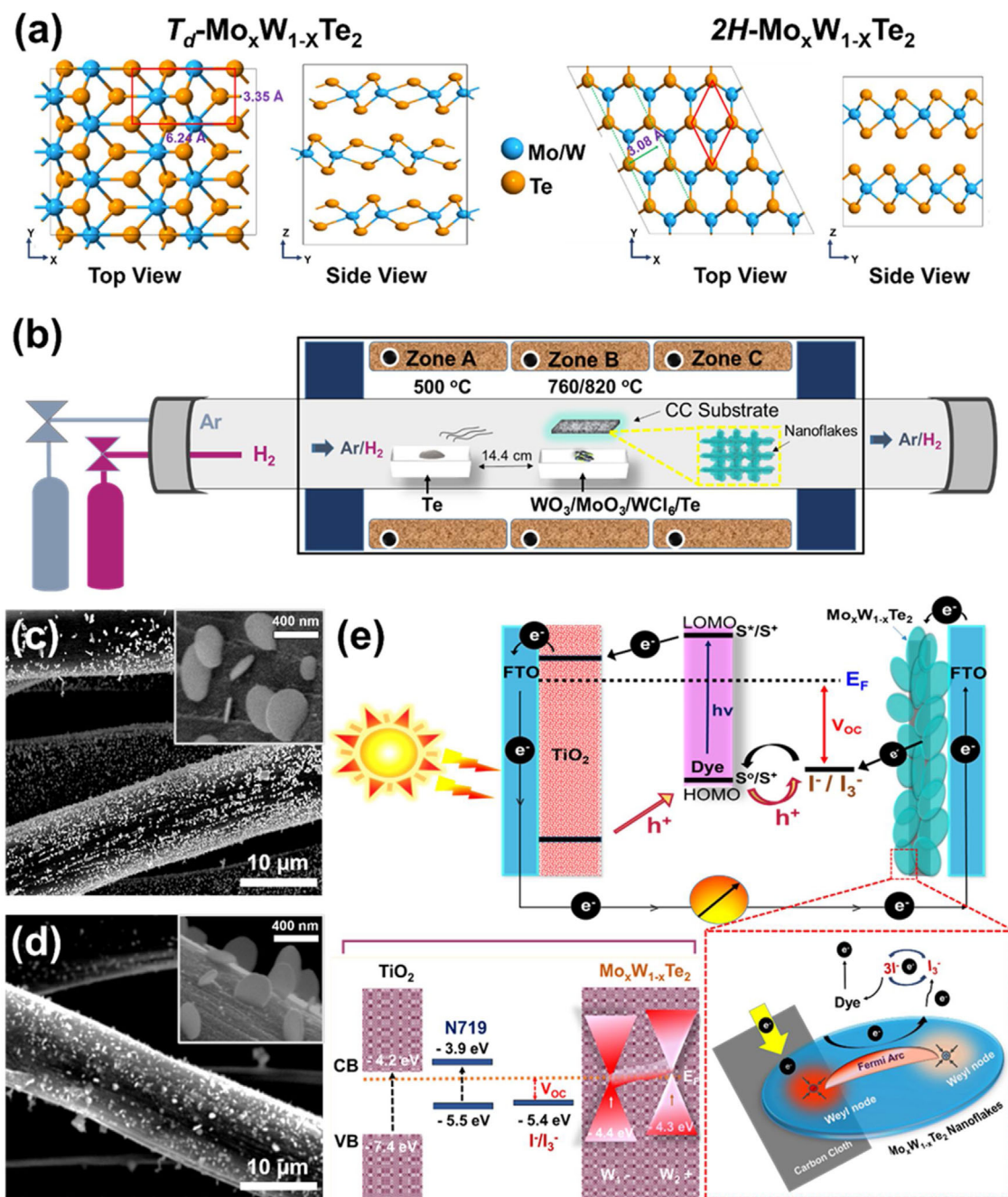
Figure 1. $Mo_xW_{1-x}Te_2$ nanosheets were synthesized to be used as an electrocatalyst for the CE of DSSC. a) The schematic crystal structures of T_d-$Mo_xW_{1-x}Te_2$ and $2H$-$Mo_xW_{1-x}Te_2$. b) A schematic illustration of the CVD synthesis process to grow $Mo_xW_{1-x}Te_2$ nanocrystals. c–d) The SEM images show the CC fibers decorated with different crystal phases of $Mo_xW_{1-x}Te_2$ nanosheets to be used as electrocatalysts in DSSC. (c) T_d- & $2H$-$Mo_{0.32}W_{0.67}Te_{2.01}$/CC was synthesized at 760 °C and (d) T_d-$Mo_{0.29}W_{0.72}Te_{1.99}$/CC was grown at 820 °C in the CVD reactions. e) A schematic representation of the TWS surface of a $Mo_xW_{1-x}Te_2$/CC used as a high-performance CE to assist the electrocatalytic reduction of I_3^- in DSSC, where S_0, S^+, and S^* represent the ground electronic state (HOMO), the hole left after light excitation, and the excited state (LUMO) of the dye molecule, respectively.

obtained at 820 °C. Figure 1b shows a schematic representation of the CVD system employed for the synthesis of $Mo_xW_{1-x}Te_2$ nanocrystals. The detailed procedures of the CVD reactions are described in Section S1 of the Supporting Information. The scanning electron microscopy (SEM) images in Figure 1c–d show the morphologies of the as-synthesized T_d- &

$2H$-$Mo_{0.32}W_{0.67}Te_{2.01}$/CC (grown at 760 °C) and T_d-$Mo_{0.29}W_{0.72}Te_{1.99}$/CC (grown at 820 °C), respectively, via different growth temperatures in the CVD reaction.

The working principle of an electrocatalytic system of DSSC using TWS $Mo_xW_{1-x}Te_2$ as a CE is represented in Figure 1e. Upon solar illumination, the photo-excited sensitizer dye (N719)

injects electrons into the conduction band of a wide-band semiconductor electrode (e.g., TiO_2 with the band gap of ≈ 3.2 eV), leaving simultaneously the oxidized dye.[42] Following the electron injection, the ground state of the dye is replenished by electrons donated from the electrolytic oxidation of $3I^- \rightarrow I_3^- + 2e-$; in return, the regeneration of I^- is driven by the electrolytic reduction of $I_3^- + 2e- \rightarrow 3I^-$ at the TWS $Mo_xW_{1-x}Te_2$ CE/electrolyte interface. The electrocatalytic activity of the overall cell can be enhanced by increasing the surface area of CE to expedite charge transfers.[21,43] The TWS $Mo_xW_{1-x}Te_2$ nanoflakes (Figure 1c–d) with the Fermi arcs between Weyl nodes of opposite chirality[44] could provide enormous electrocatalytic surface areas for charge transfer routes. In addition to driving the reduction of I_3^-, the robust TWS surface states could enhance the rapid transfer of carriers, thus detaining electron-hole recombinations. Moreover, the difference between the Fermi level of TiO_2 and the redox potential of I^-/I_3^- determines the open-circuit voltage (V_{oc}, Figure 1e) generated by the cell under solar illumination.[42]

2. Results and Discussion

In **Figure 2**a, we determined the compositions of the CVT-grown bulk crystal (black trace) and the CVD-synthesized nanocrystals at 820 °C (red trace) of $Mo_xW_{1-x}Te_2$ by X-ray photoelectron spectroscopy (XPS), where the binding energies of Mo, W, and Te were calibrated against the C 1s peak at 284.8 eV to remove the background charging current.[45] The binding energies of the nanosheets synthesized at 820 °C showed Mo $3d_{5/2}$ (227.9 eV), Mo $3d_{3/2}$ (231.1 eV), W $4f_{7/2}$ (31.2 eV), W $4f_{5/2}$ (33.4 eV), Te $3d_{5/2}$ (573.0 eV), and Te $3d_{3/2}$ (583.4 eV) with the composition ratio of $Mo_{0.29}W_{0.72}Te_{1.99}$, which is essentially the same as the CVT-grown bulk crystal of $Mo_{0.29}W_{0.71}Te_{2.0}$. According to the previously reported composition-based phase determination,[30,46] both CVT-grown bulk crystal and the CVD-synthesized nanosheets at 820 °C belong to the T_d phase (referred to as T_d-$Mo_{0.29}W_{0.71}Te_{2.0}$ and T_d-$Mo_{0.29}W_{0.72}Te_{1.99}$ hereafter).[30–32,47] In contrast, the XPS spectrum of the CVD-grown alloy crystal at 760 °C (blue trace in Figure 2a) showed the compositions of $Mo_{0.32}W_{0.67}Te_{2.01}$ to
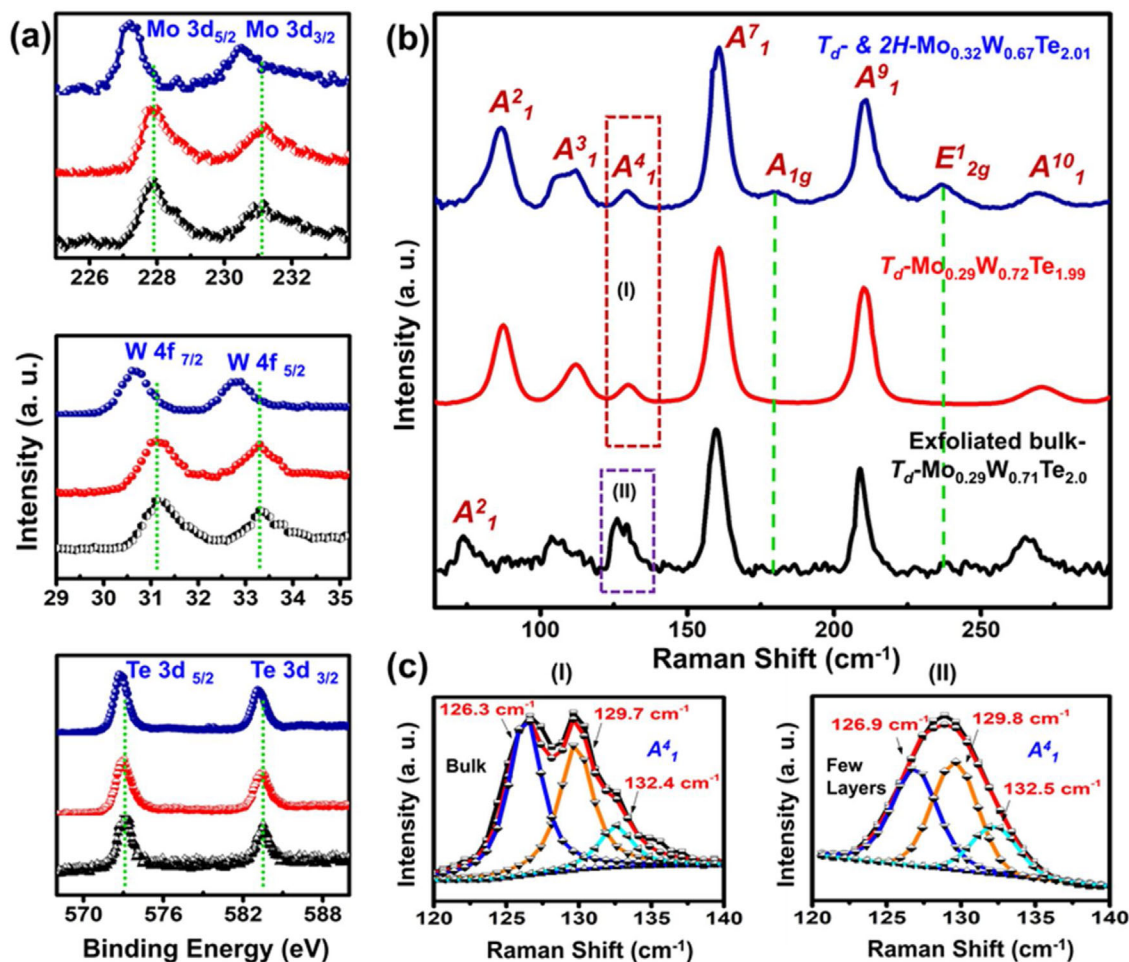

Figure 2. a) XPS spectra of the CVD-grown $Mo_xW_{1-x}Te_2$ crystals at 760 °C (blue trace) and 820 °C (red trace) together with the CVT-grown $Mo_xW_{1-x}Te_2$ bulk crystal (black trace) contain the Mo 3d levels (top panel), W 4f levels (middle panel), and Te 3d levels (bottom panel). b) Raman spectra of the CVD-grown T_d- & 2H-$Mo_{0.32}W_{0.67}Te_{2.01}$ (synthesized at 760 °C, blue trace) and T_d-$Mo_{0.29}W_{0.72}Te_{1.99}$ (synthesized at 820 °C, red trace) and the CVT-grown bulk crystal of T_d-$Mo_{0.29}W_{0.71}Te_{2.0}$ (black spectra). c) The splitting features deconvoluted from the Raman signals at 120–140 cm^{-1} indicate the alloy characteristics of (I) CVT-grown bulk and (II) CVD-synthesized T_d-$Mo_{0.29}W_{0.72}Te_{1.99}$ or T_d- & 2H-$Mo_{0.32}W_{0.67}Te_{2.01}$ nanosheets.

possess a mixed phases of T_d- & $2H$-$Mo_{0.32}W_{0.67}Te_{2.01}$. Compared with the above two crystals of T_d-phase, the binding energies of both Mo and W in T_d- & $2H$-$Mo_{0.32}W_{0.67}Te_{2.01}$ are shifted toward lower energy by 0.8 eV (Mo $3d_{5/2}$ at 227.1 eV and Mo $3d_{3/2}$ at 230.3 eV) and 0.6 eV (W $4f_{7/2}$ at 30.6 eV and W $4f_{5/2}$ at 32.8 eV), respectively (see also the XPS analysis in Figure S2, Supporting Information). A slight lower binding energy of Te $3d_{5/2}$ (572.8 eV) and Te $3d_{3/2}$ (583.2 eV) in T_d- & $2H$-$Mo_{0.32}W_{0.67}Te_{2.01}$ was also observed, albeit by much smaller shift ($\approx$0.2 eV). It is noted that a crystal of $2H$ phase exhibits lower binding energies than those of T_d and $1T'$ phases.[48] These shifts to the lower binding energies also evidence the existence of multiple crystal phases with different lattice parameters.[48]

In Figure 2b, Raman spectra of the CVD-synthesized T_d- & $2H$-$Mo_{0.32}W_{0.67}Te_{2.01}$ (blue trace) and T_d-$Mo_{0.29}W_{0.72}Te_{1.99}$ (red trace) nanosheets together with the CVT-grown T_d-$Mo_{0.29}W_{0.71}Te_{2.0}$ bulk crystal (black trace) were compared to characterize their alloy features and phase identifications. For T_d-$Mo_{0.29}W_{0.71}Te_{2.0}$ bulk crystal (black trace), A_1^2 at 74.4 cm^{-1} (A_1^2), 106.3 cm^{-1} (A_1^3), 126.3/129.7/132.4 cm^{-1} (A_1^4), 159.8 cm^{-1} (A_1^7), 209.1 cm^{-1} (A_1^9), and 266.4 cm^{-1} (A_1^{10}), of which the spectral assignments consist with the earlier reports.[30–32,40,49] Notably, the vibrational pattern of T_d-$Mo_{0.29}W_{0.72}Te_{1.99}$ nanosheets (red trace) is similar, but has a

slight blue shift, to that of T_d-$Mo_{0.29}W_{0.71}Te_{2.0}$ bulk crystal (black spectra); this blue shift is attributed to the screening of long-range Coulomb forces in the few-layered nanosheets.[50] Moreover, compared with T_d-$Mo_{0.29}W_{0.71}Te_{2.0}$ bulk crystal (black trace), the T_d-$Mo_{0.29}W_{0.72}Te_{1.99}$ nanosheets (red trace) have an enhanced intensity ratio of A_1^2 to A_1^3 or A_1^4, which also supports the characteristics of few-layered crystals and can be accounted for by the availability of multiple bands of $Mo_xW_{1-x}Te_2$ to allow electron-phonon resonance for the thickness-dependent intensities of the phonon modes involving interlayer interactions.[30–32] The peak splittings at 120–140 cm^{-1} (marked by the violet and red dotted boxes in Figure 2b and deconvoluted in Figure 2c) are caused by the inversion symmetry breaking and random metal atom substitutions in the alloy crystals.[30–32] However, the Raman spectrum of T_d- & $2H$-$Mo_{0.32}W_{0.67}Te_{2.01}$ nanosheets (blue trace in Figure 2b) exhibits two additional peaks at 179.9 cm^{-1} (A_{1g}) and 236.5 cm^{-1} (E_{2g}^1), which correspond to the phonon modes of the $2H$ crystal and once more confirm the co-existence of T_d- & $2H$-phases revealed in the above XPS analysis.[30–32,51]

The crystal structure of the as-synthesized $Mo_xW_{1-x}Te_2$ was further examined by high-resolution transmission electron microscopy (HR-TEM), selected-area electron diffraction (SAED), and energy-dispersive X-ray spectroscopy (EDS).
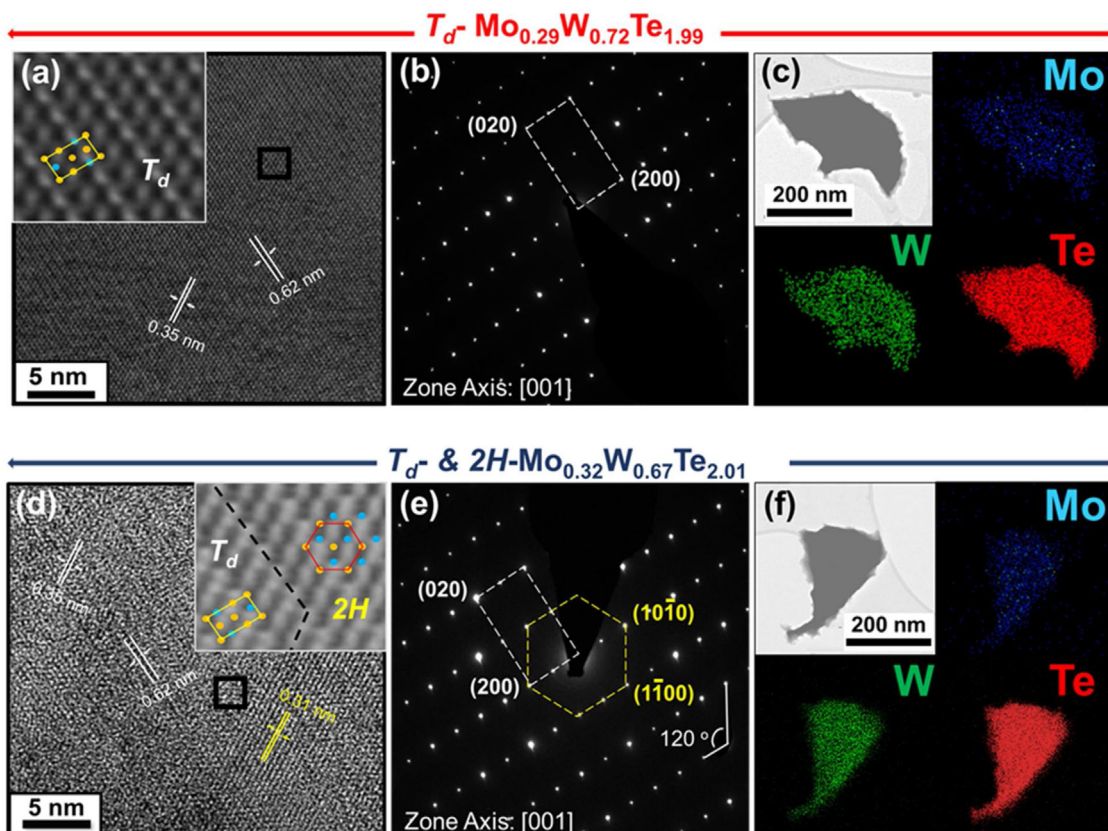

Figure 3. The HR-TEM images of (a) T_d-$Mo_{0.29}W_{0.72}Te_{1.99}$ and (d) T_d- & $2H$-$Mo_{0.32}W_{0.67}Te_{2.01}$ nanoflakes are presented. The insets show the atomically resolved lattice structures. The SAED patterns of (b) T_d-$Mo_{0.29}W_{0.72}Te_{1.99}$ and (e) T_d- & $2H$-$Mo_{0.32}W_{0.67}Te_{2.01}$ nanosheets are indexed with the [001] zone axis. EDS elemental mapping images of (c) T_d-$Mo_{0.29}W_{0.72}Te_{1.99}$ and (f) T_d- & $2H$-$Mo_{0.32}W_{0.67}Te_{2.01}$ nanoflakes are displayed. The insets show the TEM images of the alloy nanosheets analyzed.

Figure 3a shows the HR-TEM image of T_d-$Mo_{0.29}W_{0.72}Te_{1.99}$ nanosheets (CVD-synthesized at 820 °C) to possess the orthorhombic lattice with the interplanar spacings of 6.2 and 3.5 Å for the (100) and (010) planes, respectively. [35] Figure 3b displays the SAED pattern of the orthorhombic T_d-$Mo_{0.29}W_{0.72}Te_{1.99}$ indexed using [001] zone axis. In sharp contrast, Figure 3d shows the mixed lattice structures of T_d- & $2H$-$Mo_{0.32}W_{0.67}Te_{2.01}$ nanosheets (CVD-synthesized at 760 °C), where the hexagonal ($10\bar{1}0$) and ($1\bar{1}00$) lattice planes ($d = 3.1$ Å) appeared in addition to the orthorhombic (100) and (010) planes ($d = 6.2$ and 3.5 Å, respectively). Similarly, the SAED patterns (Figure 3e) of T_d- & $2H$-$Mo_{0.32}W_{0.67}Te_{2.01}$ nanosheets display both orthorhombic (020) and (200) lattice planes and hexagonal ($10\bar{1}0$) and ($1\bar{1}00$) lattice planes. The perfectly matched lattice parameters and diffraction patterns of the T_d- & $2H$-crystals further confirm the co-existence of two crystal phases in T_d- & $2H$-$Mo_{0.32}W_{0.67}Te_{2.01}$. The EDS elemental mapping images of T_d-$Mo_{0.29}W_{0.72}Te_{1.99}$ (Figure 3c) and T_d- & $2H$-$Mo_{0.32}W_{0.67}Te_{2.01}$ (Figure 3f) indicate the homogeneous distributions of the chemical compositions of Mo, W, and Te in the alloy nanosheets.

For measuring the electric transports in $Mo_xW_{1-x}Te_2$ nanocrystals, we also synthesized large-sized $Mo_xW_{1-x}Te_2$ thin films on a silicon wafer following the same synthesis procedures as the aforementioned growth of $Mo_xW_{1-x}Te_2$/CC. To differentiate the electric transport properties of T_d-$Mo_{0.29}W_{0.72}Te_{1.99}$ and T_d- & $2H$-$Mo_{0.32}W_{0.67}Te_{2.01}$, field-effect transistors (FET, **Figure 4**a) fabricated with these two alloyed nanocrystals as the conducting channels (≈ 4 nm in thickness and 15 μm in length) were investigated, respectively. The transfer curves of the as-fabricated FETs reveal clearly the semi-metallic behavior of T_d-$Mo_{0.29}W_{0.72}Te_{1.99}$-FET (Figure 4b) and the p-type semiconducting property of T_d- & $2H$-$Mo_{0.32}W_{0.67}Te_{2.01}$-FET (Figure 4c). Notably, the semi-metallic T_d-$Mo_{0.29}W_{0.72}Te_{1.99}$-FET has higher output current than the semiconducting T_d- & $2H$-$Mo_{0.32}W_{0.67}Te_{2.01}$-FET by multiple times as the same gate voltage was applied. Further electronic properties of the CVD-grown $Mo_xW_{1-x}Te_2$ nanocrystals were evaluated by four-probe Hall effect measurements under 0.55 T magnetic field at 300 K (Figures 4d and e and S4, Supporting Information). The carrier density of T_d-$Mo_{0.29}W_{0.72}Te_{1.99}$ ($n = (1.59 \pm 0.04) \times 10^{20}$ cm^{-3}) was determined ≈ 10 times higher than that of T_d- & $2H$-$Mo_{0.32}W_{0.67}Te_{2.01}$ ($n = (1.20 \pm 0.02) \times 10^{19}$ cm^{-3}). Similarly, the charge mobility of $\mu = 385.47 \pm 10.9$ cm^2 V^{-1} s^{-1} in T_d-$Mo_{0.29}W_{0.72}Te_{1.99}$ is also significantly higher than $\mu = (276.11 \pm 7.8$ cm^2 V^{-1} s$^{-1})$ in the counterpart of T_d- & $2H$-$Mo_{0.32}W_{0.67}Te_{2.01}$. It is important to note that the high carrier density and mobility in the CE of DSSC are essential for the electrocatalytic redox reactions, where a dense flow of migrating charge carriers can trigger rapid charge transfers at the CE/electrolyte interface to enhance the reaction kinetics.[21–22] As the electrochemical application illustrated in Figure 1e, various CVD-grown $Mo_xW_{1-x}Te_2$ nanocrystals were employed as different CEs in DSSC to compare their electrocatalytic activities.

In electrocatalytic applications, T_d-$Mo_{0.29}W_{0.72}Te_{1.99}$/CC and T_d- & $2H$-$Mo_{0.32}W_{0.67}Te_{2.01}$/CC were used as CEs of DCCS to compare with a standard Pt catalyst sputtered on CC (denoted by Pt/CC). The SEM images and EDS elemental mappings (Figure S5, Supporting Information in Section S5) show the uniform $Mo_xW_{1-x}Te_2$ nanosheets or Pt film decorated on the CC

surface. The vertically aligned $Mo_xW_{1-x}Te_2$ nanosheets on CC surface could augment the surface area of CE to catalyze the reduction reaction of I_3^- ions at the CE/electrolyte interface and thereby facilitate the regeneration of the oxidized dye for detaining the recombination of photo-generated electron-hole pairs.[6] The electrocatalytic activities of the CEs fabricated with bare CC, T_d-$Mo_{0.29}W_{0.72}Te_{1.99}$/CC, T_d- & $2H$-$Mo_{0.32}W_{0.67}Te_{2.01}$/CC, and Pt/CC (referred to as the four tested CEs hereafter) in DSSC were measured by cyclic voltammetry (CV) using a three-electrode system in an electrochemical cell with the electrolyte containing the I^-/I_3^- redox couple. In these measurements, the higher cathodic peak current density (J_{PC}) represents the better apparent electrocatalytic activity for the I_3^- reduction; besides, the peak separation between the oxidation and reduction peaks (ΔE_P) varies inversely with the intrinsic heterogeneous charge-transfer rate constant (k^0).[52–54] **Figure 5**a shows the measured CV curves of the four tested CEs with their electrochemical parameters listed in **Table 1**, where the J_{PC} relating to the reduction of the I_3^- ions follows an order of T_d-$Mo_{0.29}W_{0.72}Te_{1.99}$/CC ($-2.72$ mA cm^{-2}) > T_d- & $2H$-$Mo_{0.32}W_{0.67}Te_{2.01}$/CC ($-2.45$ mA cm^{-2}) > Pt/CC (-2.03 mA cm^{-2}) >> bare CC. The ΔE_P for the redox reaction of I^-/I_3^- follows an order of Pt/CC (427 mV) $\approx$ T_d-$Mo_{0.29}W_{0.72}Te_{1.99}$/CC (429 mV) < T_d- & $2H$-$Mo_{0.32}W_{0.67}Te_{2.01}$/CC (461 mV) << bare CC. For the $Mo_xW_{1-x}Te_2$-based electrodes, T_d-$Mo_{0.29}W_{0.72}Te_{1.99}$/CC exhibits the higher J_{PC} and smaller ΔE_P than T_d- & $2H$-$Mo_{0.32}W_{0.67}Te_{2.01}$/CC, indicating the better electrocatalytic ability of T_d-$Mo_{0.29}W_{0.72}Te_{1.99}$/CC.

In addition to the topologically protected nature, the high carrier density ($n = (1.59 \pm 0.04) \times 10^{20}$ cm^{-3}) and mobility ($\mu = [385.47 \pm 10.9$ cm^2 V^{-1} s$^{-1}]$) of semi-metallic T_d-$Mo_{0.29}W_{0.72}Te_{1.99}$ nanosheets could promote the rapid charge transfers, resulting in the higher J_{PC} (-2.72 mA cm^{-2}) and smaller ΔE_P (429 mV) values. In contrast, the semiconducting $2H$ crystal in a T_d- & $2H$-$Mo_{0.32}W_{0.67}Te_{2.01}$/CC CE could exacerbate the TWS characteristics by reducing the carrier density and electrocatalytic activity, resulting in the larger ΔE_P (461 mV) than those of other electrodes. Notably, the J_{PC} values of both T_d-$Mo_{0.29}W_{0.72}Te_{1.99}$/CC and T_d- & $2H$-$Mo_{0.32}W_{0.67}Te_{2.01}$/CC are higher than that of Pt/CC, which could stem from the vertically aligned nanosheets on the CC surfaces to provide vast exchange sites for interfacial charge transfers to assist the redox reaction, whereas the catalytic area of the Pt/CC electrode was limited only to the surface area of the CC substrate. The more favorable performance of T_d-$Mo_{0.29}W_{0.72}Te_{1.99}$/CC than Pt/CC, that is, the similar ΔE_P but higher J_{PC}, makes the TWS alloyed crystal a strong candidate to replace Pt in electrocatalysis.

Next, the four tested CEs were employed for DSSC to examine their solar cell performances. The measured photocurrent density versus voltage (J–V) curves are shown in Figure 5b and their corresponding photovoltaic parameters are summarized in **Table 2**. The DSSC with bare CC shows a poor cell efficiency (η) of 0.48%. After the deposition of T_d- & $2H$-$Mo_{0.32}W_{0.67}Te_{2.01}$ on CC, the η was greatly enhanced to 7.81%, comparable to 8.01% of a Pt/CC CE-based DSSC. By using a T_d-$Mo_{0.29}W_{0.72}Te_{1.99}$/CC CE, the η of the corresponding DSSC could be further improved to 8.85%, which is $ca.$ 10% higher than that of the cell using a Pt/CC CE (8.01%). Obviously, the performance tests reveal that T_d-$Mo_{0.29}W_{0.72}Te_{1.99}$/CC, as a CE in DSSC, acts better than T_d- &
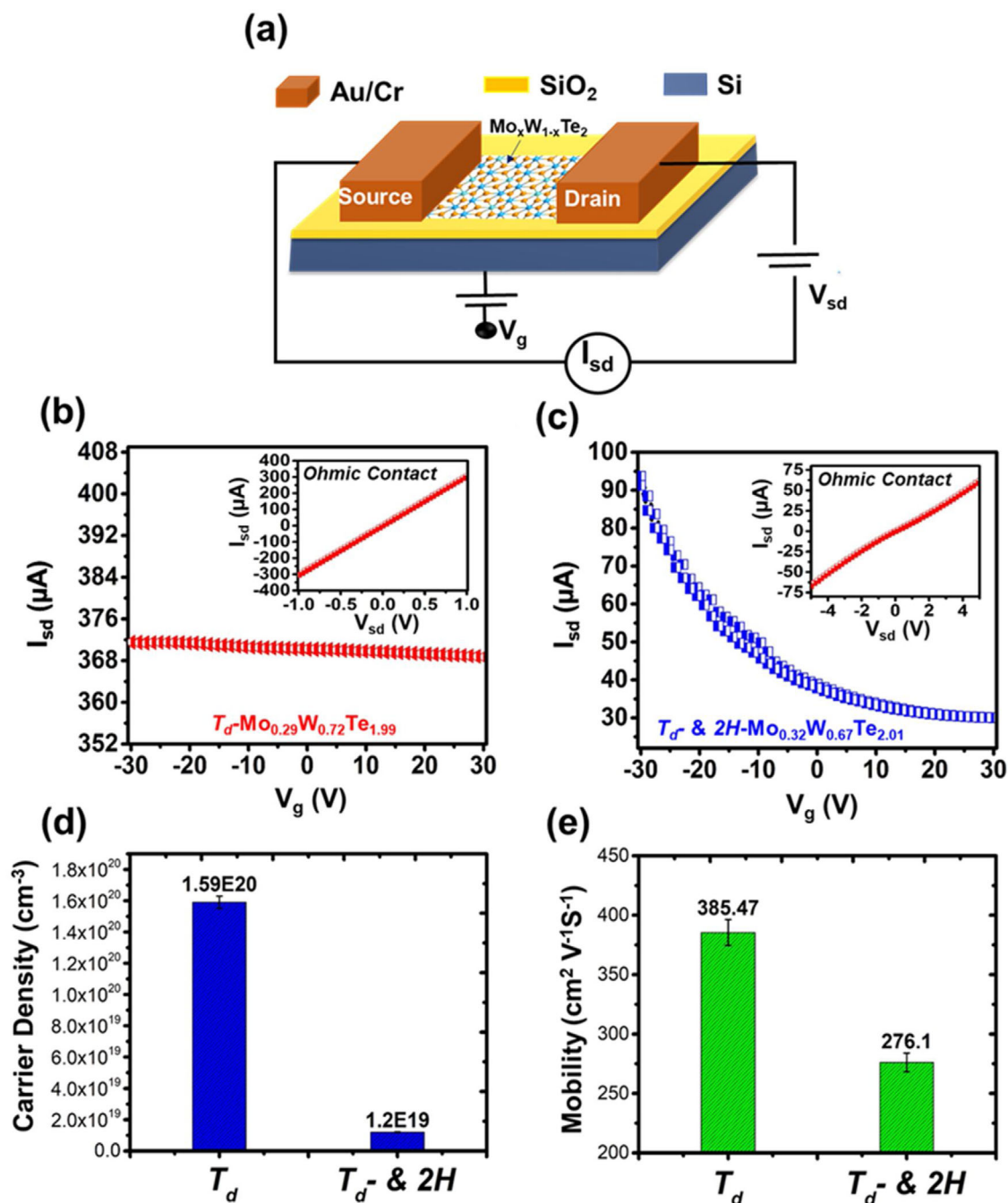
Figure 4. a) A schematic illustration of the as-fabricated FET device using the CVD-synthesized $Mo_xW_{1-x}Te_2$ nanocrystal as a conducting channel. b–c) The electrical transport properties of $Mo_xW_{1-x}Te_2$-based FETs were measured in vacuum at ≈ 10 mTorr. c) The transfer curve of a T_d-$Mo_{0.29}W_{0.72}Te_{1.99}$-FET exhibits the semi-metallic behavior. The inset presents the measured output curve of the as-fabricated device to have an ohmic contact with the resistivity of $(1.1 \pm 0.3) \times 10^{-4}\,\Omega\,cm$. c) The transfer curve of a T_d- & $2H$-$Mo_{0.32}W_{0.67}Te_{2.01}$-FET shows the p-type semiconducting behavior. The inset shows the measured output curve to have an ohmic contact with the resistivity of $(1.9 \pm 0.5) \times 10^{-3}\,\Omega\,cm$. The (d) carrier density and (e) mobility of the devices fabricated with T_d-$Mo_{0.29}W_{0.72}Te_{1.99}$ and T_d- & $2H$-$Mo_{0.32}W_{0.67}Te_{2.01}$ were obtained from four-probe Hall effect measurements.

$2H$-$Mo_{0.32}W_{0.67}Te_{2.01}$/CC and Pt/CC. Figure 5c shows the incident photo-to-electron conversion efficiency (IPCE) measurements of the DSSC using the four tested CEs, in which all of the IPCE curves exhibit their broad spectral coverage at 400–800 nm; their calculated photocurrent densities (J_{IPCE}) were summarized in Table 2 by integrating IPCE with the AM 1.5G solar spectrum. The J_{IPCE} values of DSSC obtained from the uses of bare CC, T_d- & $2H$-$Mo_{0.32}W_{0.67}Te_{2.01}$/CC, T_d-
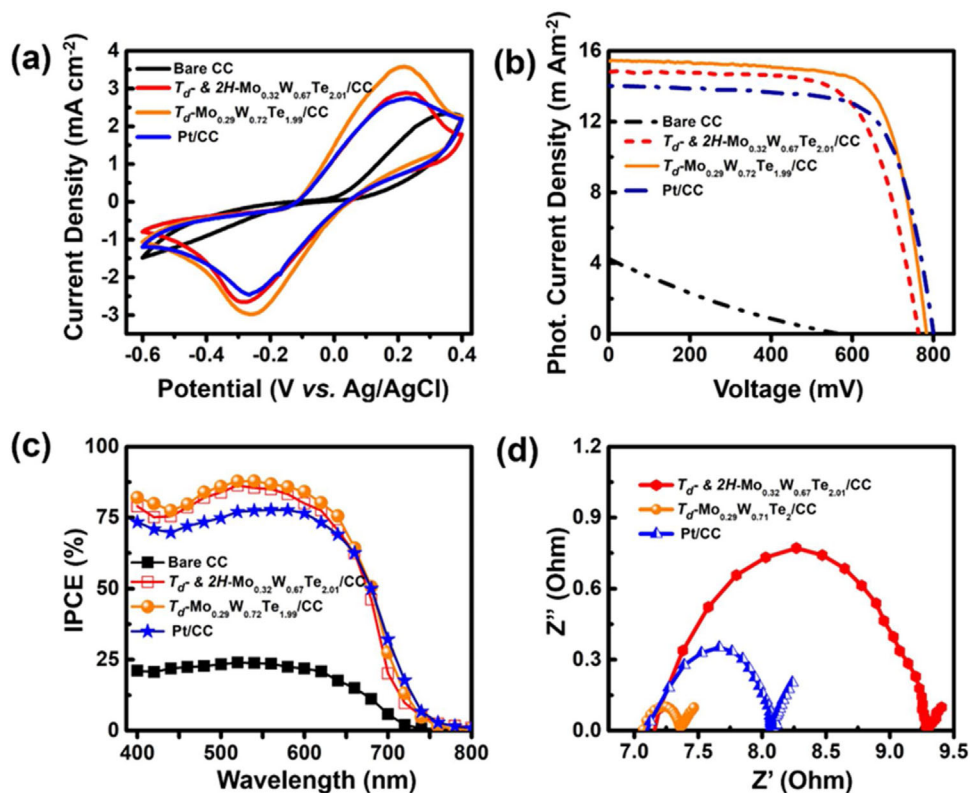
Figure 5. Various electrochemical activities of the bare CC, T_d-$Mo_{0.29}W_{0.72}Te_{1.99}$/CC, T_d- & $2H$-$Mo_{0.32}W_{0.67}Te_{2.01}$/CC, and Pt/CC electrodes were tested. a) The CV measurements in a three-electrode electrochemical system. b) The $J-V$ curves under AM 1.5G illumination at 100 mW cm^{-2}. c) The IPCE curves of DSSC. d) The EIS of the symmetrical dummy cells consisted of two identical electrodes were measured at 0 V from 100 kHz to 10 mHz.

$Mo_{0.29}W_{0.72}Te_{1.99}$/CC, and Pt/CC are 3.92, 14.53, 15.16, and 13.94 mA cm^{-2}, respectively; these values agree well with the J_{SC} values acquired from the $J-V$ curves (Figure 4b and Table 2). Most importantly, the $M_xW_{1-x}Te_2$-based CEs exhibited much higher incident photo-to-current conversion efficiency (>87%) than Pt CE ($\approx$75%) and the bare CC (<25%). This indicates that the superior electro-catalytic ability of $M_xW_{1-x}Te_2$ could greatly promote the IPCE value of a DSSC device, which stems from the topologically protected Weyl semi-metallic properties, as mentioned in the previous paragraphs.

Furthermore, electrochemical impedance spectroscopy (EIS) was used to investigate the interfacial charge-transfer kinetics in the four tested CEs by using a symmetric cell consisting of the same electrocatalyst on both anode and cathode. In general, the EIS spectrum of a symmetric dummy cell shows two semi-circles in the measured frequency range. The first and second semi-

circles correspond to the charge-transfer resistances occurring at the electrocatalytic electrode/electrolyte interface (R_{ct1}) and the Warburg diffusion process of I^-/I_3^- ions in the electrolyte ($R_{diff.}$), respectively. As shown in Figure 5d, the R_{ct1} values of the electrocatalytic electrodes show a tendency of T_d-$Mo_{0.29}W_{0.72}Te_{1.99}$/CC < Pt/CC < T_d- & $2H$-$Mo_{0.32}W_{0.67}Te_{2.01}$/CC. A symmetric cell with lower R_{ct1} implies the less loss of internal energy at the electrode/electrolyte interface during the electrocatalytic process[55]; accordingly, the reduction reaction of I_3^- (i.e., $I_3^- + 2e^- \rightarrow 3I^-$) can work more efficiently at the electrocatalytic electrode. Therefore, the lowest R_{ct1} value is responsible for the greatest efficiency of DSSC by using the CE of T_d-$Mo_{0.29}W_{0.72}Te_{1.99}$/CC.

Finally, we tested the long-term stabilities of the CEs fabricated with T_d- & $2H$-$Mo_{0.32}W_{0.67}Te_{2.01}$/CC, T_d-$Mo_{0.29}W_{0.72}Te_{1.99}$/CC, and Pt/CC, respectively, by conducting 200-cycle continuous CV measurements in the I^-/I_3^- redox reaction as shown in Figure S6a–c, Supporting Information. In general, for a stable electrocatalytic electrode, there should be neither an obvious change in the CV curves after the potential is scanned consecutively, nor a detectable change in the peak current density as the cycle number is increased. Figure S6d, Supporting Information shows the cycle number dependence of J_{PC} (i.e., the cathodic current density of the I_3^- reduction reaction) extracted from Figure S6a–c, Supporting Information where the J_{PC} values of T_d- & $2H$-$Mo_{0.32}W_{0.67}Te_{2.01}$/CC and T_d-$Mo_{0.29}W_{0.72}Te_{1.99}$/CC remain almost constant after 200-cycle CV

Table 1. The measured electrochemical parameters by CV using various electrodes.

Electrodes	J_{PC} [mA cm^{-2}]	$\triangle E_P$ [mV]
Bare CC	–	–
T_d- & $2H$-$Mo_{0.32}W_{0.67}Te_{2.01}$/CC	−2.45	461
T_d-$Mo_{0.29}W_{0.72}Te_{1.99}$/CC	−2.72	429
Pt/CC	−2.03	427

**ADVANCED
SCIENCE NEWS**

www.advancedsciencenews.com

Solar
RRL

www.solar-rrl.com

Table 2. The photovoltaic parameters of DSSC with various CEs measured at $100\,mW\,cm^{-2}$ (AM 1.5G) light intensity.

Counter electrodes	η [%]	V_{OC} [mV]	J_{SC} [mA cm^{-2}]	FF	J_{IPCE} [mA cm^{-2}]
Bare CC	0.48	566	4.28	0.20	3.92
T_d- & $2H$-Mo$_{0.32}$W$_{0.67}$Te$_{2.01}$/CC	7.81	762	14.83	0.69	14.53
T_d-Mo$_{0.29}$W$_{0.72}$Te$_{1.99}$/CC	8.85	782	15.44	0.73	15.16
Pt/CC	8.01	800	14.04	0.71	13.94

scans; in contrast, the Pt/CC decreases obviously in the test, likely resulting from the surface contamination and the Pt-dissolving issue in the I^-/I_3^- electrolyte.[37] This result reveals that the robustly protected TWS surface states of $Mo_xW_{1-x}Te_2$-based CEs (i.e., T_d- & $2H$-Mo$_{0.32}$W$_{0.67}$Te$_{2.01}$/CC and T_d-Mo$_{0.29}$W$_{0.72}$Te$_{1.99}$/CC) possess excellent electrocatalytic durability over 200 redox cycles in the I^-/I_3^- electrolyte.

Acting as a CE in DSSC, the performance of $Mo_xW_{1-x}Te_2$/CC was compared with that of a recently reported CVD-synthesized $MoTe_2$ thin film. For a $MoTe_2$ CE, the maximal η of 7.25% was reported under the solar illumination of $100\,mW\,cm^{-2}$ (AM 1.5 G solar spectrum). As a reference, $\eta = 8.15\%$ was reported for a Pt/CC CE in DSSC.[56] Nevertheless, we demonstrated in this study that a T_d-Mo$_{0.29}$W$_{0.72}$Te$_{1.99}$/CC CE can achieve $\eta = 8.85\%$, which exceeds a Pt/CC CE ($\eta = 8.01\%$) and a T_d- & $2H$-Mo$_{0.32}$W$_{0.67}$Te$_{2.01}$/CC CE ($\eta = 7.81\%$). Undoubtedly, the cost-effective and structurally stable TWS T_d-Mo$_{0.29}$W$_{0.72}$Te$_{1.99}$ possesses the highly efficient performance and excellent durability in electrocatalysis and becomes a promising candidate to replace Pt in electrocatalytic reactions.

3. Conclusion

In conclusion, highly crystalline $Mo_xW_{1-x}Te_2$ nanosheets were successfully synthesized directly on CC via CVD reactions. Controlling the growth temperature plays a key role to engineer the crystal phases, which were identified by the Raman, XPS, HR-TEM, and SAED measurements. Comparatively, the electric transport of semi-metallic T_d-Mo$_{0.29}$W$_{0.72}$Te$_{1.99}$ showed much higher charge-carrier density and mobility than T_d- & $2H$-Mo$_{0.32}$W$_{0.67}$Te$_{2.01}$. Furthermore, the CV measurement of T_d-Mo$_{0.29}$W$_{0.72}$Te$_{1.99}$/CC exhibited the highest cathodic peak current density ($J_{PC} = -2.72\,mA\,cm^{-2}$) relative to T_d- & $2H$-Mo$_{0.32}$W$_{0.67}$Te$_{2.01}$/CC ($J_{PC} = -2.45\,mA\,cm^{-2}$) and Pt/CC ($J_{PC} = -2.03\,mA\,cm^{-2}$). The highly active T_d-Mo$_{0.29}$W$_{0.72}$Te$_{1.99}$ alloy could efficiently promote the charge transport in the I^-/I_3^- redox reaction, resulting in superior electrocatalytic performance. Meanwhile, the stability of $Mo_xW_{1-x}Te_2$-based CEs has been demonstrated over 200-cycle CV scans in the I^-/I_3^- electrolyte, which could not be achieved by a Pt/CC electrode. As a CE of DSSC, the $\eta = 8.85\%$ achieved by T_d-Mo$_{0.29}$W$_{0.72}$Te$_{1.99}$/CC is better than Pt/CC (8.01%) and T_d- & $2H$-Mo$_{0.32}$W$_{0.67}$Te$_{2.01}$/CC-CE (7.81%). The tendency of the charge-transfer resistance at the electrode/electrolyte interface (R_{ct1}) shows a trend of T_d-Mo$_{0.29}$W$_{0.72}$Te$_{1.99}$/CC < Pt/CC < T_d- & $2H$-Mo$_{0.32}$W$_{0.67}$Te$_{2.01}$/CC, indicating the lowest internal energy loss of a semi-metallic T_d-Mo$_{0.29}$W$_{0.72}$Te$_{1.99}$/CC at the electrode/electrolyte interface. Consequently, this work shows the potential of applying TWS materials for developing a cost-effective, highly efficient, and stable catalyst

for the Pt-free DSSC. This study also inspires further investigations of TWSs for extensive electrocatalytic applications.

4. Experimental Section

Crystal Synthesis: $Mo_xW_{1-x}Te_2$ nanosheets were synthesized directly on CC (CC-W0S1002, CeTech Co., Ltd., Taiwan; thickness: 360 μm, basic weight: 120 g cm^{-2}, and sheet resistance: 0.63 Ω sq^{-1}) in CVD reactions using a three-zone fractional heating furnace system (Thermocraft Incorporated) with a quartz reaction tube of 2 cm in diameter. Prior to the deposition of $Mo_xW_{1-x}Te_2$ nanoflakes on CC, the CC substrates were cleaned by soaking them into H_2SO_4 (18 M, Sigma–Aldrich) for 1 week and then washed sequentially with deionized water, ethanol, and isopropanol. While a boat containing a mixture of MoO_3, WO_3, WCl_6, and Te (99.99% in purity for all samples, Sigma–Aldrich) with a calculated molar ratio was located in the middle of the quartz reaction tube, another boat containing an excess of Te powder was placed on the upstream side of the furnace system. The phase transition between T_d-Mo$_{0.29}$W$_{0.72}$Te$_{1.99}$ and T_d- & $2H$-Mo$_{0.32}$W$_{0.67}$Te$_{2.01}$ could be controlled by adjusting the growth temperatures at 820 and 760 °C, respectively, with the heating rate of 20.5 and 22.2 °C min^{-1}. The reaction time of the alloy growth was lasted for 7 min under atmospheric pressure with a flow of 50 sccm Ar and 7 sccm H$_2$ to catalyze the reduction of metal oxides, followed by slow cooling to room temperature. The reaction processes related with the growth of $Mo_xW_{1-x}Te_2$ nanoflakes are proposed in the Supporting Information. To prepare Pt/CC as a standard CE, a cleaned CC substrate was deposited with a Pt layer by direct current (DC) sputtering. All of the samples were annealed before further characterizations.

Growth of $Mo_{0.29}W_{0.71}Te_{2.0}$ Bulk Crystal: Bulky $Mo_{0.29}W_{0.71}Te_{2.0}$ single crystal was synthesized by CVT using iodine as the transporting agent. A quartz tube, containing W and Mo powders as metal sources and Te pellets as a chalcogen source, was heated at 1150 °C for 11 days with a temperature gradient of ≈100 °C day^{-1}. Subsequently, the tube was cooled down to 1050 °C at the rate of 10 °C h^{-1}; a further cooling rate of 2 °C h^{-1} was followed for 2 days until 800 °C. Finally, a quenching step was conducted under atmospheric conditions.

Structural Characterizations: Chemical configurations of the as-synthesized crystals were determined by XPS (ESCALAB 250, VG Scientific) coupled with 1486.6 eV Al Kα monochromatic X-ray source, where the biding energies were calibrated against the C 1s peak.[57] Raman spectra were acquired with a 532 nm laser as an excitation source in a confocal Raman spectrometer (LabRAM HR, Horiba) with the Si signal at 520 cm^{-1} as a calibration peak. Lattice structures of the as-grown crystals were examined by HR-TEM (Philips Tacnai-G2 F30, accelerating voltage of 300 kV), equipped with X-ray energy dispersive spectroscopy (EDS). Surface morphologies of the as-grown nanoflakes were observed by a field-emission SEM (FEI Nova 200), equipped with EDS.

Fabrication of FET Devices: Few-layer $Mo_xW_{1-x}Te_2$-based FET devices were fabricated using the CVD-synthesized $Mo_xW_{1-x}Te_2$ as a conducting channel (≈4 nm in thickness and 15 μm in length). For the deposition of Cr/Au (5 nm/50 nm) electrodes by thermal evaporation, a TEM copper grid, used as a shadow mask, was mounted on the $Mo_xW_{1-x}Te_2$ nanocrystal with the assistance of a homemade micro-manipulator.[58] The electrical parameters of the as-fabricated devices were measured in a probe station (TTPX, Lakeshore) equipped with a source meter (2636A, Keithley). The transfer curves ($I_{ds}–V_g$) were recorded at V_g scanned from

−30 to 30 V at $V_{ds} = 1$ V under a vacuum condition of ≈10 mTorr. The output curves (I_{sd}–V_{sd}) were measured at V_{sd} scanned from −1 to +1 V. The four-probe Hall effect measurements were conducted in a Van der Pauw Ecopia HMS-3000 Hall Measurement System at 300 K with the applied magnetic field of 0.55 T.

Electrochemical Measurements: To investigate the electrocatalytic activities of the four tested CEs for the redox reaction of I^-/I_3^-, CV measurements were carried out in a potentiostat/galvanostat (PGSTAT 30, Autolab Eco–Chemie) with a three-electrode electrochemical system. Each of the tested samples was used as a working electrode along with a Ag/AgCl reference electrode and a Pt foil CE in the acetonitrile (ACN, 99.99%, Sigma–Aldrich) electrolyte solution, containing 10 mM LiI (synthetic grade, Merck), 1 mM I_2 (synthetic grade, Merck), and 0.1 M $LiClO_4$ (≥98.0%, Sigma–Aldrich).

Fabrication of DSSCs: A TiO_2 photoanode, containing a compact layer, a transparent layer, and a scattering layer, was deposited on a conducting glass substrate of fluorine-doped SnO_2 (FTO, TEC-7, 10 Ω sq^{-1}, NSG America Inc.). Initially, the FTO was cleaned with a neutral cleaner, followed by sequentially washing with deionized water, acetone, and isopropyl alcohol. Consecutively, a compact layer (≈100 nm in thickness) was prepared on the cleaned FTO substrate by spin-coating with a precursor solution, containing titanium isopropoxide (>98%, Sigma–Aldrich) and 2-methoxyethanol (99.8%, Sigma–Aldrich) in the 1:3 weight ratio, to obtain a good mechanical contact between the conducting glass and TiO_2 film. A transparent layer of ≈10 μm in thickness was then coated on the as-prepared compact layer by a doctor blade technique with a commercial transparent TiO_2 paste of an average diameter of ≈13 nm (Ti-nanoxide, Solaronix). Likewise, a scattering layer (≈4 μm in thickness) was then coated on the transparent layer with the same doctor blade technique using a home-made scattering paste. Before the next TiO_2 coating, each layer was sintered at 500 °C for 30 min in an ambient environment. Subsequently, the as-prepared TiO_2 electrode was immersed in a dye solution of 5×10^{-4} M N719 (Solaronix S.A.), containing a mixed solvent of acetonitrile and tert-butyl alcohol (in the 1:1 volume ratio), at room temperature for 24 h. Finally, the $Mo_xW_{1-x}Te_2$ nanosheets/CC CE was firstly coupled with a dye-sensitized TiO2 photoanode. These two electrodes were separated by a 25 μm-thick Surlyn® film (SX1170–25, Solaronix S.A., Aubonne, Switzerland), and then a bare FTO substrate was attached on the back-side of the W1-xMoxTe2 nanosheets/CC, where the photoanode, CE, and bare FTO were fixed together by folders. Subsequently, the electrolyte was injected into the gap between the dye-sensitized TiO2 photoanode and the bare FTO substrate by capillary. Finally, a DSSC was prepared for the measurements. A mixture of solution was used as the electrolyte, containing 1.2 M 1,2-dimethyl-3-propylimidazolium iodide (Solaronix SA), 0.35M I_2 (synthetic grade, Merck), 0.1 M thiocyanate guanidine (99%, Sigma–Aldrich), and 0.5 M 4-tertbutylpyridine (96%, Acros) in acetonitrile/3-methoxypropionitrile (99%, Acros) with the volume ratio of 8:2.

DSSC Measurements: The surface of the DSSC was illuminated by a class A quality solar simulator (XES-301S, AM 1.5G, SAN-EI ELECTRIC CO., LTD.). The intensity of incident light (100 mW cm^{-2}) was calibrated with a standard Si cell (PECSI01, Peccell Technologies, Inc., Yokohama, Japan). Photoelectrochemical characteristics of the DSSC were recorded with a potentiostat/galvanostat (PGSTAT 30, Autolab, Eco–Chemie, the Netherlands). The IPCE curves were obtained at the short-circuit condition. The light source was a class A quality solar simulator (PEC-L11, AM1.5G, Peccell Technologies, Inc.); light was focused through a monochromator (Oriel Instrument, model 74100) onto the photovoltaic cell. The monochromator was incremented through the visible spectrum to generate the IPCE (λ) as defined by

$$IPCE(\lambda) = 1240 \left(J_{SC}/\lambda_\varphi \right)$$

where λ is the wavelength, J_{SC} is the short-circuit photocurrent density (mA cm^{-2}) recorded with a potentiostat/galvanostat, and φ is the incident radiative flux (W m^{-2}) measured with an optical detector (Oriel Instrument, model 71580), and a power meter (Oriel Instrument, model 70310).

The light source was provided by a class A quality solar simulator (AM 1.5 G, XES-301S, San-Electroic Co. LTD) with the incident light intensity of 100 mW cm^{-2}, which was calibrated with a standard Si cell (PECSI01, Peccell Technologies Inc.). The photoelectrochemical and electrochemical impedance spectra, scanned from 100 kHz to 10 mHz at 0 V, were recorded with a potentiostat/galvanostat equipped with an FRA2 module. The IPCE curves were obtained at the short-circuit condition using another class A quality solar simulator (PEC-L11, AM1.5G, Peccell Technologies, Inc.), which was focused through a monochromator (model 74100, Oriel Instrument) onto the photovoltaic cell.

Supporting Information

Supporting Information is available from the Wiley Online Library or from the author.

Acknowledgement

Conflicts of Interest

The authors declare no conflict of interest.

Keywords

[1] H. Li, C. Tsai, A. L. Koh, L. Cai, A. W. Contryman, A. H. Fragapane, J. Zhao, H. S. Han, H. C. Manoharan, F. Abild-Pedersen, J. K. Nørskov, X. Zheng, *Nat. Matter.* **2015**, *15*, 48.

[2] M. Chhowalla, H. S. Shin, G. Eda, L. J. Li, K. P. Loh, H. Zhang, *Nat. Chem.* **2013**, *5*, 263.

[3] Z. Jin, M. Zhang, M. Wang, C. Feng, Z.-S. Wang, *Acc. Chem. Res.* **2017**, *50*, 895.

[4] J. Zhang, S. Najmaei, H. Lin, J. Lou, *Nanoscale* **2014**, *6*, 5279.

[5] C. Tsai, H. Li, S. Park, J. Park, H. S. Han, J. K. Nørskov, X. Zheng, F. Abild-Pedersen, *Nat. Commun.* **2017**, *8*, 15113.

[6] D. Deng, K. S. Novoselov, Q. Fu, N. Zheng, Z. Tian, X. Bao, *Nat. Nanotechnol.* **2016**, *11*, 218.

[7] R. D. Nikam, A.-Y. Lu, P. A. Sonawane, U. R. Kumar, K. Yadav, L.-J. Li, Y.-T. Chen, *ACS Appl. Mater. Interfaces* **2015**, *7*, 23328.

[8] L. R. L. Ting, Y. Deng, L. Ma, Y.-J. Zhang, A. A. Peterson, B. S. Yeo, *ACS Catal.* **2016**, *6*, 861.

[9] G. Li, D. Zhang, Q. Qiao, Y. Yu, D. Peterson, A. Zafar, R. Kumar, S. Curtarolo, F. Hunte, S. Shannon, Y. Zhu, W. Yang, L. Cao, *J. Am. Chem. Soc.* **2016**, *138*, 16632.

[10] S. Jinbong, L. Jun-Ho, C. Suyeon, J. Byungdo, K. Hyo Won, K. Min, K. Dohyun, K. Young-Min, O. Sang Ho, K. Sung Wng, L. Young Hee, S. Young-Woo, Y. Heejun, *2D Mater.* **2017**, *4*, 025061.

[11] S.-Y. Xu, N. Alidoust, I. Belopolski, Z. Yuan, G. Bian, T.-R. Chang, H. Zheng, V. N. Strocov, D. S. Sanchez, G. Chang, C. Zhang, D. Mou, Y. Wu, L. Huang, C.-C. Lee, S.-M. Huang, B. Wang, A. Bansil, H.-T. Jeng, T. Neupert, A. Kaminski, H. Lin, S. Jia, M. Zahid Hasan, *Nat. Phys.* **2015**, *11*, 748.

[12] L. X. Yang, Z. K. Liu, Y. Sun, H. Peng, H. F. Yang, T. Zhang, B. Zhou, Y. Zhang, Y. F. Guo, M. Rahn, D. Prabhakaran, Z. Hussain, S. K. Mo, C. Felser, B. Yan, Y. L. Chen, *Nat. Phys.* **2015**, *11*, 728.

[13] H. Weng, C. Fang, Z. Fang, B. A. Bernevig, X. Dai, *Phys. Rev. X* **2015**, *5*, 011029.

[14] A. A. Soluyanov, D. Gresch, Z. Wang, Q. Wu, M. Troyer, X. Dai, B. A. Bernevig, *Nature* **2015**, *527*, 495.

[15] K. Deng, G. Wan, P. Deng, K. Zhang, S. Ding, E. Wang, M. Yan, H. Huang, H. Zhang, Z. Xu, J. Denlinger, A. Fedorov, H. Yang, W. Duan, H. Yao, Y. Wu, S. Fan, H. Zhang, X. Chen, S. Zhou, *Nat. Phys.* **2016**, *12*, 1105.

[16] S. Jia, S. Y. Xu, M. Z. Hasan, *Nat. Mater.* **2016**, *15*, 1140.

[17] L. Huang, T. M. McCormick, M. Ochi, Z. Zhao, M. T. Suzuki, R. Arita, Y. Wu, D. Mou, H. Cao, J. Yan, N. Trivedi, A. Kaminski, *Nat. Mater.* **2016**, *15*, 1155.

[18] T. R. Chang, S. Y. Xu, G. Chang, C. C. Lee, S. M. Huang, B. Wang, G. Bian, H. Zheng, D. S. Sanchez, I. Belopolski, N. Alidoust, M. Neupane, A. Bansil, H. T. Jeng, H. Lin, M. Zahid Hasan, *Nat. Commun.* **2016**, *7*, 10639.

[19] D. H. Keum, S. Cho, J. H. Kim, D.-H. Choe, H.-J. Sung, M. Kan, H. Kang, J.-Y. Hwang, S. W. Kim, H. Yang, K. J. Chang, Y. H. Lee, *Nat. Phys.* **2015**, *11*, 482.

[20] K. Kazuaki, N. Zeyuan, A. Ryuichi, S. Tetsuroh, L. Chun-Liang, M. Emi, W. Satoshi, K. Maki, T. Noriaki, *Appl. Phys. Express* **2017**, *10*, 045702.

[21] C. R. Rajamathi, U. Gupta, N. Kumar, H. Yang, Y. Sun, V. Süß, C. Shekhar, M. Schmidt, H. Blumtritt, P. Werner, B. Yan, S. Parkin, C. Felser,* and C. N. R. Rao*, *Adv. Mater.* **2017**, *29*, 1606202.

[22] J. Li, H. Ma, Q. Xie, S. Feng, S. Ullah, R. Li, J. Dong, D. Li, Y. Li, X.-Q. Chen, *Sci. China Mater.* **2018**, *61*, 23.

[23] H. Chen, W. Zhu, D. Xiao, Z. Zhang, *Phys. Rev. Lett.* **2011**, *107*, 056804.

[24] K. J. Manoj, S. Anjali, J. L. Dattatray, R. R. Catherine, B. Kanishka, F. Claudia, V. W. Umesh, C. N. R. Rao, *J. Phys.: Condens. Matter* **2015**, *27*, 285401.

[25] M. Trescher, E. J. Bergholtz, M. Udagawa, J. Knolle, *Phys. Rev. B* **2017**, *96*, 201101.

[26] Y. Nakata, K. Sugawara, S. Ichinokura, Y. Okada, T. Hitosugi, T. Koretsune, K. Ueno, S. Hasegawa, T. Takahashi, T. Sato, *npj 2D Mater. Appl.* **2018**, *2*, 12.

[27] J.-V. Wezel, P. Littlewood, *Physics* **2010**, *3*, 87.

[28] S. Yun, P. D. Lund, A. Hinsch, *Energy Environ. Sci.* **2015**, *8*, 3495.

[29] C. Tan, H. Zhang, *Nat. Commun.* **2015**, *6*, 7873.

[30] S. M Oliver, S. Krylyuk, I. Kalish, A. K Singh, A. Bruma, F. Tavazza, J. Joshi, I. R. Stone, S. J Stranick, A. V Davydov, P. M Vora, *2D Mater.* **2017**, *4*, 045008.

[31] M. Yamamoto, S. T. Wang, M. Ni, Y.-F. Lin, S.-L. Li, S. Aikawa, W.-B. Jian, K. Ueno, K. Wakabayashi, K. Tsukagoshi, *ACS Nano* **2014**, *8*, 3895.

[32] T. Goldstein, S.-Y. Chen, J. Tong, D. Xiao, A. Ramasubramaniam, J. Yan, *Sci. Rep.* **2016**, *6*, 28024.

[33] B. E. Brown, *Acta Cryst.* **1966**, *20*, 268.

[34] Y. Qi, P. G. Naumov, M. N. Ali, C. R. Rajamathi, W. Schnelle, O. Barkalov, M. Hanfland, S.-C. Wu, C. Shekhar, Y. Sun, V. Süß, M. Schmidt, U. Schwarz, E. Pippel, P. Werner, R. Hillebrand, T. Förster, E. Kampert, S. Parkin, R. J. Cava, C. Felser, B. Yan, S. A. Medvedev, *Nat. Commun.* **2016**, *7*, 11038.

[35] I. Belopolski, D. S. Sanchez, Y. Ishida, X. Pan, P. Yu, S.-Y. Xu, G. Chang, T.-R. Chang, H. Zheng, N. Alidoust, G. Bian, M. Neupane, S.-M. Huang, C.-C. Lee, Y. Song, H. Bu, G. Wang, S. Li, G. Eda, H.-T. Jeng, T. Kondo, H. Lin, Z. Liu, F. Song, S. Shin, M. Z. Hasan, *Nat. Commun.* **2016**, *7*, 13643.

[36] H.-W. C. Chung-Wei Kung, C.-Y. Lin, K.-C. Huang, R. Vittal, K.-C. Ho, *ACS Nano* **2012**, *6*, 7016.

[37] M. Wu, T. Ma, *ChemSusChem* **2012**, *5*, 1343.

[38] J. C. Park, H. Kim, J. H. Park, S H Chae, S.-J An, J.-G Kim, S. M Kim, K. K. Kim, Y. H. Lee, *ACS Nano* **2015**, *9*, 6548.

[39] A. A. Al-Hilli, B. L. Evans, *J. Cryst. Growth* **1972**, *15*, 93.

[40] J. Zhou, F. Liu, J. Lin, X. Huang, J. Xia, B. Zhang, Q. Zeng, H. Wang, C. Zhu, L. Niu, X. Wang, W. Fu, P. Yu, T. R. Chang, C. H. Hsu, D. Wu, H. T. Jeng, Y. Huang, H. Lin, Z. Shen, C. Yang, L. Lu, K. Suenaga, W. Zhou, S. T. Pantelides, G. Liu, Z. Liu, *Adv. Mater.* **2017**, *29*, 1603471.

[41] L. Zhou, K. Xu, A. Zubair, A. D. Liao, W. Fang, F. Ouyang, Y. H. Lee, K. Ueno, R. Saito, T. Palacios, J. Kong, M. S. Dresselhaus, *J. Am. Chem. Soc.* **2015**, *137*, 11892.

[42] A. Listorti, B. O'Regan, J. R. Durrant, *Chem. Mater.* **2011**, *23*, 3381.

[43] Y. Hou, D. Wang, X. H. Yang, W. Q. Fang, B. Zhang, H. F. Wang, G. Z. Lu, P. Hu, H. J. Zhao, H. G. Yang, *Nat. Commun.* **2013**, *4*, 1583.

[44] B. Yang, Q. Guo, B. Tremain, L. E. Barr, W. Gao, H. Liu, B. Béri, Y. Xiang, D. Fan, A. P. Hibbins, S. Zhang, *Nat. Commun.* **2017**, *8*, 97.

[45] M. J. Mleczko, R. L. Xu, K. Okabe, H.-H. Kuo, I. R. Fisher, H. S. P. Wong, Y. Nishi, E. Pop, *ACS Nano* **2016**, *10*, 7507.

[46] C. H. Naylor, W. M. Parkin, J. Ping, Z. Gao, Y. R. Zhou, Y. Kim, F. Streller, R. W. Carpick, A. M. Rappe, M. Drndić, J. M. Kikkawa, A. T. C. Johnson, *Nano Lett.* **2016**, *16*, 4297.

[47] D. Rhodes, D. A. Chenet, B. E. Janicek, C. Nyby, Y. Lin, W. Jin, D. Edelberg, E. Mannebach, N. Finney, A. Antony, T. Schiros, T. Klarr, A. Mazzoni, M. Chin, Y. c. Chiu, W. Zheng, Q. R. Zhang, F. Ernst, J. I. Dadap, X. Tong, J. Ma, R. Lou, S. Wang, T. Qian, H. Ding, R. M. Osgood, D. W. Paley, A. M. Lindenberg, P. Y. Huang, A. N. Pasupathy, M. Dubey, J. Hone, L. Balicas, *Nano Lett.* **2017**, *17*, 1616.

[48] S. Cho, S. Kim, J. H. Kim, J. Zhao, J. Seok, D. H. Keum, J. Baik, D.-H. Choe, K. J. Chang, K. Suenaga, S. W. Kim, Y. H. Lee, H. Yang, *Science* **2015**, *349*, 625.

[49] X. Ma, P. Guo, C. Yi, Q. Yu, A. Zhang, J. Ji, Y. Tian, F. Jin, Y. Wang, K. Liu, T. Xia, Y. Shi, Q. Zhang, *Phys. Rev. B* **2016**, *94*, 214105.

[50] R. Beams, L. G. Cançado, S. Krylyuk, I. Kalish, B. Kalanyan, A. K. Singh, K. Choudhary, A. Bruma, P. M. Vora, F. Tavazza, A. V. Davydov, S. J. Stranick, *ACS Nano* **2016**, *10*, 9626.

[51] R. Sankar, G. Narsinga Rao, I. P. Muthuselvam, C. Butler, N. Kumar, G. Senthil Murugan, C. Shekhar, T.-R. Chang, C.-Y. Wen, C.-W. Chen, W.-L. Lee, M. T. Lin, H.-T. Jeng, C. Felser, F. C. Chou, *Chem. Mater.* **2017**, *29*, 699.

[52] S. Hou, X. Cai, H. Wu, X. Yu, M. Peng, K. Yan, D. Zou, *Energy Environ. Sci.* **2013**, *6*, 3356.

[53] W. Li, C. Tan, M. A. Lowe, H. D. Abruña, D. C. Ralph, *ACS Nano* **2011**, *5*, 2264.

[54] C.-P. Lee, K.-Y. Lai, C.-A. Lin, C.-T. Li, K.-C. Ho, C.-I. Wu, S.-P. Lau, J.-H. He, *Nano Energy* **2017**, *36*, 260.

[55] C.-P. Lee, C.-A. Lin, T.-C. Wei, M.-L. Tsai, Y. Meng, C.-T. Li, K.-C. Ho, C.-I. Wu, S.-P. Lau, J.-H. He, *Nano Energy* **2015**, *18*, 109.

[56] S. Hussain, S. A. Patil, D. Vikraman, N. Mengal, H. Liu, W. Song, K.-S. An, S. H. Jeong, H.-S. Kim, J. Jung, *Sci. Rep.* **2018**, *8*, 29.

[57] R. D. Nikam, P. A. Sonawane, R. Sankar, Y.-T. Chen, *Nano Energy* **2017**, *32*, 454.

[58] P. Perumal, R. K. Ulaganathan, R. Sankar, Y.-M. Liao, T.-M. Sun, M.-W. Chu, F. C. Chou, Y.-T. Chen, M.-H. Shih, Y.-F. Chen, *Adv. Funct. Mater.* **2016**, *26*, 3630.

Supporting Information

Phase-Engineered Weyl Semi-metallic $Mo_xW_{1-x}Te_2$ Nanosheets as a Highly Efficient Electrocatalyst for Dye-Sensitized Solar Cells

Shemsia Mohammed Hudie, Chuan-Pei Lee, Roshan Jesus Mathew, Tzu-En Chien, Yi-June Huang, Han-Ting Chen, Kuo-Chuan Ho, Chi-Ang Tseng, and Yit-Tsong Chen*

S.M. Hudie, C.-A. Tseng, T.-E. Chien, Y.-T. Chen
Department of Chemistry, National Taiwan University, No. 1, Section 4, Roosevelt Road, Taipei 10617, Taiwan.

C.-P. Lee
Department of Applied Physics and Chemistry, University of Taipei, Taipei 10048, Taiwan.

S.M. Hudie, R. J. M., T.-E. Chien, C.-A. Tseng, Y.-T. Chen
Institute of Atomic and Molecular Sciences, Academia Sinica, P.O. Box 23-166, Taipei 106, Taiwan.

S.M. Hudie, R. J. Mathew
Nano-Science and Technology Program, Taiwan International Graduate Program, Academia Sinica, No. 128, Section 2, Academia Rd, Nangang, Taipei, 11529, Taiwan.

Y.-J. Huang, H.-T. Chen, K.-C. Ho
Department of Chemical Engineering, National Taiwan University, Taipei 10617, Taiwan.

R. J. Mathew
Department of Engineering & System Sciences, National Tsing-Hua University, Hsinchu, Taiwan.

* Corresponding Author: ytcchem@ntu.edu.tw; +886-2-3366-8193

Content

Section S1. Synthesis of $Mo_xW_{1-x}Te_2$ Nanocrystals

S1A. Crystal Synthesis Method

The CVD synthesis of $Mo_xW_{1-x}Te_2$ nanosheets was carried out using carbon cloth (CC) as growth substrates. While Te powder, used as the Te source, was placed at Zone A of the quartz tube in the CVD furnace (see **Figure 1b** of the main text), a mixture of MoO_3, WO_3, WCl_6, and Te (prepared with a calculated molar ratio) in a ceramic boat, used as the Mo and W sources, was located at Zone B. Several growth substrates were laid on top of the ceramic boats at Zone B. Prior to the deposition of $Mo_xW_{1-x}Te_2$ nanosheets on CC (denoted by $Mo_xW_{1-x}Te_2$/CC), the CC substrates were cleaned by soaking them into concentrated H_2SO_4 (18 M) for one week and then washed sequentially with deionized water, ethanol, and isopropanol.

The temporal temperature profiles in a CVD reaction for the growth of $Mo_xW_{1-x}Te_2$ nanosheets are illustrated in **Figure S1a**. The source samples at Zone B were first heated to 150 °C in 7 min and kept there for another 5 min to clean the substrate surface from adsorbed moisture or particles through a continuous flow of 50 sccm Ar carrier gas. Subsequently, both the Te source at Zone A and the mixture of MoO_3, WO_3, WCl_6, and Te sources at Zone B were heated simultaneously to 500 °C and 760 °C (or 820 °C), respectively, in 37 min. Meanwhile, a flow of H_2 gas (7 sccm) was introduced to assist the reduction of metal oxides in the reaction. The growth reaction was lasted for 7 min under an atmospheric pressure. After the synthetic reactions, while the product resulting from the reaction at 760 °C was characterized to be *T_d*- & *2H*-$Mo_{0.32}W_{0.67}Te_{2.01}$, the product from 820 °C was identified as *T_d*-$Mo_{0.29}W_{0.72}Te_{1.99}$.

Besides the very small difference in the electronegativities between Mo/W and Te (by ~0.3–0.4 eV only), another unique feature of telluride compounds, e.g., $Mo_xW_{1-x}Te_2$, is the very small energy differences (<0.1 eV) among various crystal phases, such as semiconductive *2H* and

semi-metallic *1T'* or T_d.[S1] We synthesized the desired crystal structures of $Mo_xW_{1-x}Te_2$ by controlling the experimental conditions of crystal growth, especially the growth temperature. We obtained a pure T_d phase of $Mo_xW_{1-x}Te_2$ nanosheets (identified as T_d-$Mo_{0.29}W_{0.72}Te_{1.99}$ by XPS analysis) at 820 °C with a heating rate of 22.2 °C min^{-1}, while a mixture of crystal phases (identified as T_d- & *2H*-$Mo_{0.32}W_{0.67}Te_{2.01}$ by XPS analysis) was obtained at 760 °C with a heating rate of 20.5 °C min^{-1}. Thus, different crystal phases of $Mo_xW_{1-x}Te_2$ could be modulated by controlling the growth conditions, where the T_d phase of $Mo_xW_{1-x}Te_2$ crystal could be obtained at fast growth kinetics, while the *2H* phase crystal was favored at slow reaction kinetics.[S2]
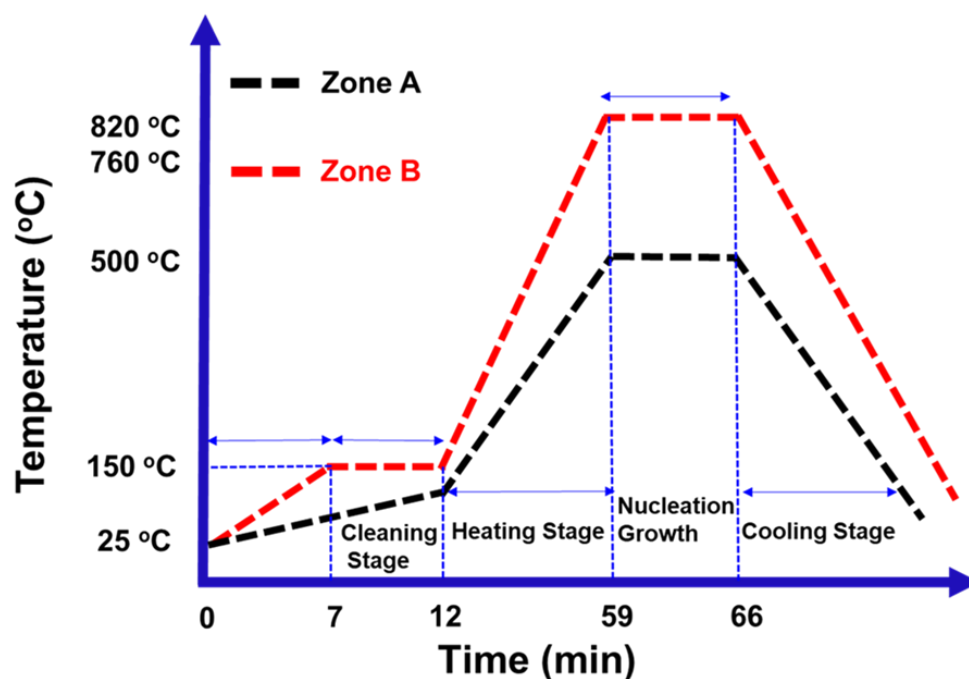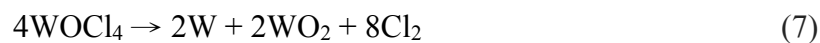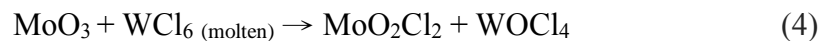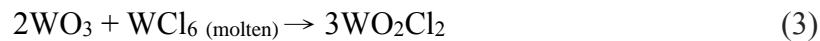

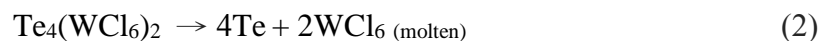**Figure S1.** The temporal temperature profiles in the CVD reactions for the growth of T_d-$Mo_{0.29}W_{0.72}Te_{1.99}$ nanosheets at 820 °C or T_d- & *2H*-$Mo_{0.32}W_{0.67}Te_{2.01}$ nanosheets at 760 °C.

S1B. Chemical Reactions

The temperature-dependent phase engineering of $Mo_xW_{1-x}Te_2$ nanosheets in the CVD reactions can be categorized into five major stages, including (a) the formation and decomposition of the Te-WCl_6 complex, (b) the formation of metal oxychlorides, (c) the decomposition of metal oxychlorides into their reduced states, (d) the formation of reactive metal-Te species, and (e) the termination step.

In step (a), the Te vapor interacted with WCl_6 at 190–230 $^{\circ}C$ to form $Te_4(WCl_6)_2$ at Zone B as described on Eq. (1). The $Te_4(WCl_6)_2$ complex was stable only at <230 $^{\circ}C$ and decomposed to elemental Te and molten WCl_6 at >230 $^{\circ}C$ (Eq. (2)). With the molten WCl_6, further reactions could be promoted in step (b) at >275 $^{\circ}C$,[S3] where the molten WCl_6 reacted with MoO_3 and WO_3 to form the metal oxychlorides of MoO_2Cl_2, WO_2Cl_2, and $WOCl_4$ as shown in Eqs. (3)–(4). These reactive metal oxychlorides were stable only at <350 $^{\circ}C$.[S4] In step (c), the decomposition of metal oxychlorides occurred at >350 $^{\circ}C$ and finally yielded the reduced states of MoO_3 or WO_3 in the forms of MoO_2 and WO_2 (Eqs. (5)–(7)).[S4b]

$$4Te + 2WCl_6 \rightarrow Te_4(WCl_6)_2 \tag{1}$$

$$Te_4(WCl_6)_2 \rightarrow 4Te + 2WCl_{6\ (molten)} \tag{2}$$

$$2WO_3 + WCl_{6\ (molten)} \rightarrow 3WO_2Cl_2 \tag{3}$$

$$MoO_3 + WCl_{6\ (molten)} \rightarrow MoO_2Cl_2 + WOCl_4 \tag{4}$$

$$MoO_2Cl_2 \rightarrow MoO_2 + Cl_2 \tag{5}$$

$$WO_2Cl_2 \rightarrow WO_2 + Cl_2 \tag{6}$$

$$4WOCl_4 \rightarrow 2W + 2WO_2 + 8Cl_2 \tag{7}$$

In step (d), the formation of metal-tellurides took place at Zone B. After Te was vaporized at ~451 °C, a fraction of MoO_2 or WO_2 (denoted by MO_2 with M = Mo or W) was dissolved into the Te vapor cloud and later reduced to free metals by H_2, thermodynamically through the eutectic point of MO_2 and Te (Eq. (8)).[S5] In the reaction, the Te source from Zone A was supplied continuously to keep abundant Te vapor at Zone B. Meanwhile, to further reduce the MO_2 and maintain the tellurization time, H_2 was introduced at 700 °C (for the growth of *T_d*- & *2H*-$Mo_{0.32}W_{0.67}Te_{2.01}$ nanosheets at 760 °C) or at 760 °C (for the growth of *T_d*-$Mo_{0.29}W_{0.72}Te_{1.99}$ nanosheets at 820 °C) to react with Te to yield H_2Te (Eq. (9)), leading to further form reactive M-Te (M = Mo or W, Eq. (10)).

$$MO_2 + 2H_{2\ (g)} \rightarrow M_{(s)} + 2H_2O \qquad (8)$$

$$2Te + H_{2\ (g)} \rightarrow H_2Te \qquad (9)$$

$$M + H_2Te \rightarrow M\text{-}Te + H_{2\ (g)} \qquad (10)$$

$$Mo\text{-}Te + W\text{-}Te \rightarrow Mo_xW_{1-x}Te_2 \qquad (11)$$

$$Cl_2 + H_2 \rightarrow 2HCl_{(g)} \qquad (12)$$

In the termination step (e), $Mo_xW_{1-x}Te_2$ nanosheets were formed on CC at 760 °C/820 °C (Eq. (11)). Furthermore, all the chloride gas, evolved during the decompositions of metal oxychlorides (Eqs. (5)–(7)), could be removed by introducing H_2 to form the HCl gas (Eq. (12)).[S6] Generally, the reactions for synthesizing $Mo_xW_{1-x}Te_2$ can be summarized as

$$MoO_3 + WO_3 + WCl_6 + 3Te + 10H_2 \rightarrow Mo_xW_{1-x}Te_2 + H_2Te_{(g)} + 6HCl_{(g)} + 6H_2O_{(g)} \quad (13)$$

After the growth reaction, all samples were annealed at 400 °C for 15 min before further characterizations. In this study, $Mo_xW_{1-x}Te_2$ thin films were also grown on Si/SiO_2 substrates following the same synthesis procedures as the aforementioned growth of $Mo_xW_{1-x}Te_2/CC$.

Section S2. Chemical Composition Analysis by X-ray Photoelectron Spectroscopy

X-ray photoelectron spectroscopy (XPS) was conducted to determine the compositions of

the as-synthesized $Mo_xW_{1-x}Te_2$ nanosheets. The binding energies of the CVD-synthesized

nanosheets (grown at 820 ^{o}C) were identified to be Mo $3d_{5/2}$ (227.9 eV), Mo $3d_{3/2}$ (231.1 eV) (**Figure S2a**), W $4f_{7/2}$ (31.2 eV), W $4f_{5/2}$ (33.4 eV) (**Figure S2b**), Te $3d_{5/2}$ (573.0 eV), and Te $3d_{3/2}$ (583.4 eV) (**Figure S2c**) with the stoichiometric composition ratio of $Mo_{0.29}W_{0.72}Te_{1.99}$. Similarly, the composition ratio of the CVT-grown bulk crystal was determined to be $Mo_{0.29}W_{0.71}Te_{2.0}$. According to the composition-based phase determination reported previously, the analyzed compositions of the bulk crystal ($Mo_{0.29}W_{0.71}Te_{2.0}$) and the as-synthesized nanosheets at 820 ^{o}C ($Mo_{0.29}W_{0.72}Te_{1.99}$) are both attributed to the semi-metallic T_d phase,[S7] denoted by T_d-$Mo_{0.29}W_{0.71}Te_{2.0}$ and T_d-$Mo_{0.29}W_{0.72}Te_{1.99}$, respectively.

In contrast, the alloyed nanosheets grown at 760 ^{o}C possess the stoichiometric composition ratio of $Mo_{0.32}W_{0.67}Te_{2.01}$ analyzed form XPS spectra (**Figures S2d−f**) and hold a mixture of semiconductive (*2H*) and semi-metallic (*T_d*) crystal phases.[S7] Compared with the binding energies of T_d-$Mo_{0.29}W_{0.72}Te_{1.99}$ (synthesized at 820 ^{o}C, **Figures S2a−b**), the observed signals of Mo $3d_{5/2}$ (227.2 eV), Mo $3d_{3/2}$ (230.3 eV) (shown in **Figure S2d**), W $4f_{7/2}$ (30.6 eV), and W $4f_{5/2}$ (32.8 eV) (displayed in **Figure S2e**) of T_d- & *2H*-$Mo_{0.32}W_{0.67}Te_{2.01}$ (grown at 760 ^{o}C) have shifted towards the lower energies by 0.7 ± 0.1 eV. Similarly, the observed Te $3d_{5/2}$ (572.8 eV), and Te $3d_{3/2}$ (583.2 eV) levels of T_d- & *2H*-$Mo_{0.32}W_{0.67}Te_{2.01}$ (**Figure S2f**) also exhibit a slight shift to the lower energy by ~0.2 eV. The shifts towards lower binding energies indicate the difference in lattice parameters.[S8] It is important to mention that the *2H* phase of $Mo_xW_{1-x}Te_2$ crystal has lower binding energies than those of T_d and *1T'* phases.[S8] Moreover, according to the phase diagram-based studies,[S7] while the *2H* phase of $Mo_xW_{1-x}Te_2$ crystal is favorable under an excessive Te content at the synthesis temperature of ~760 ^{o}C,[S9] the T_d phase is most stable under an excessive W content.[S7a] Consequently, both *2H* and T_d phases co-exist in the $Mo_{0.32}W_{0.67}Te_{2.01}$ nanosheets synthesized at 760 ^{o}C.
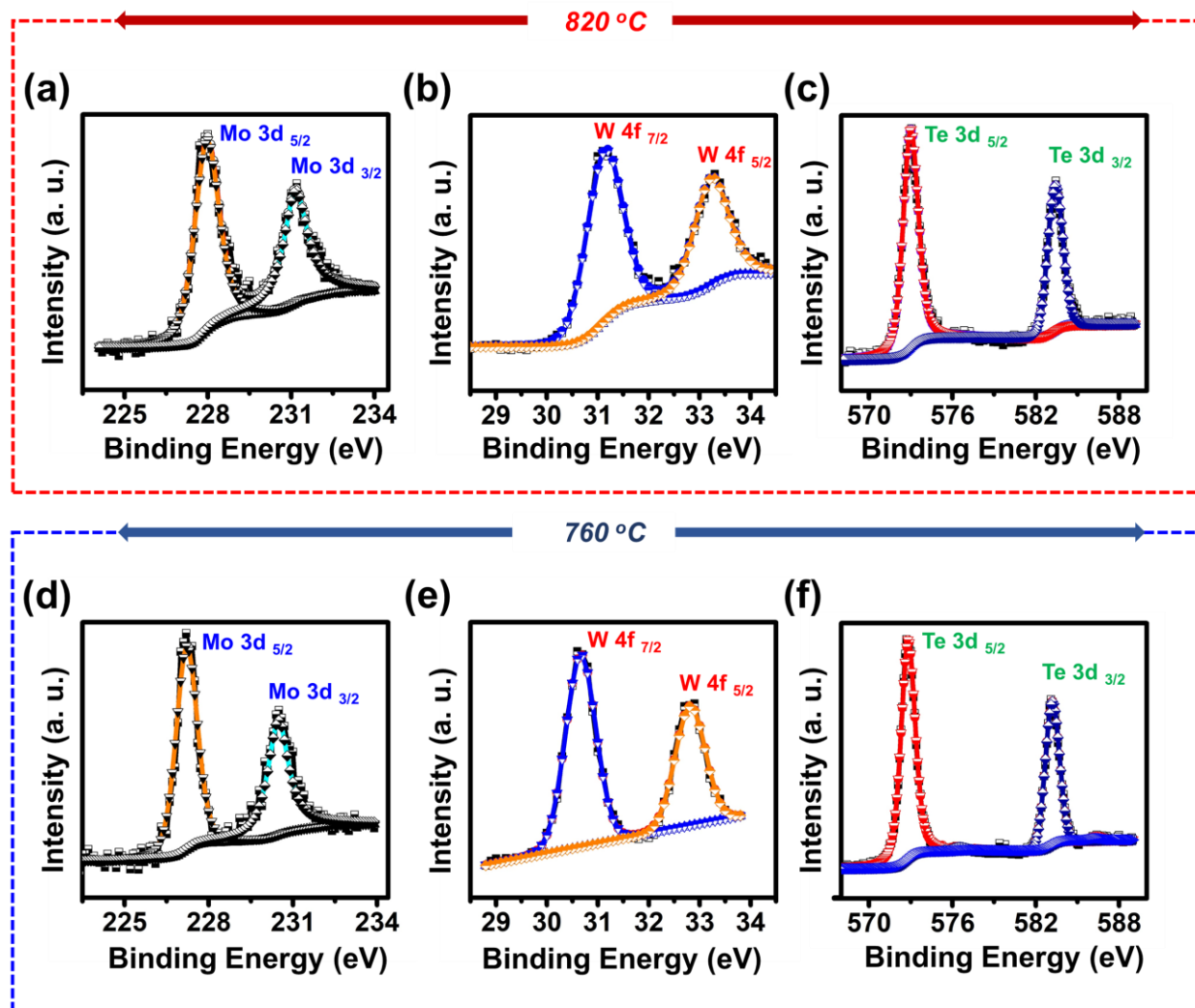
Figure S2. The XPS spectra of the $Mo_xW_{1-x}Te_2$ nanosheets synthesize in the CVD reactions at (a–c) 820 °C and (d–f) 760 °C were observed, in which the core levels of Mo are identified at (a) and (d), W at (b) and (e), and Te at (c) and (e).

Section S3. Raman Characterization

The Raman spectra of the CVD-synthesized $Mo_xW_{1-x}Te_2$ nanosheets were observed using a 532 nm laser as an excitation source. The structural stability of the as-synthesized $Mo_xW_{1-x}Te_2$ crystals could last for at least two months as demonstrated by Raman investigation. Shown in **Figure S3** are the phonon modes of T_d-$Mo_{0.29}W_{0.72}Te_{1.99}$ at 87 cm^{-1}(A_2^2), 111.7 cm^{-1} (A_1^3), 126.9/129.8/132.5 cm^{-1} (A_1^4), 160.6 cm^{-1} (A_1^7), 210.4 cm^{-1} (A_1^9), and 268.6 cm^{-1} (A_1^{10}), which were checked continuously within a two-month test. The fidelity of the Raman signals has demonstrated that the as-synthesized T_d-$Mo_{0.29}W_{0.72}Te_{1.99}$ crystal is of high structural stability.

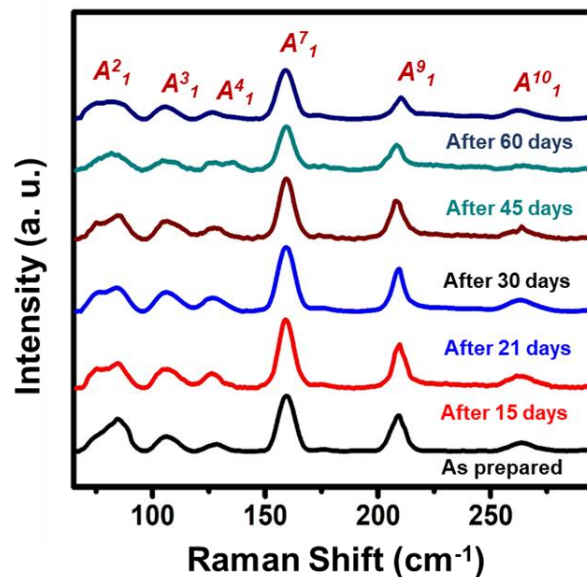**Figure S3.** The Raman spectra of the as-synthesized T_d-$Mo_{0.29}W_{0.72}Te_{1.99}$ nanocrystal show the structural stability of the alloyed material for at least two months.

Section S4. Electrical Transport Measurements for $Mo_xW_{1-x}Te_2$ of Different Crystal Phases

S4A. Hall Effect Measurements

Displayed in **Figure S4** are the four-probe Hall effect measurements of the as-synthesized $Mo_xW_{1-x}Te_2$ films (including T_d-$Mo_{0.29}W_{0.72}Te_{1.99}$ and T_d- & $2H$-$Mo_{0.32}W_{0.67}Te_{2.01}$), which were conducted under 1 mA input current and 0.55 T magnetic field. While both T_d-$Mo_{0.29}W_{0.72}Te_{1.99}$ and T_d- & $2H$-$Mo_{0.32}W_{0.67}Te_{2.01}$ show ohmic contacts between the four-probe electrodes (**Figures S4a–b**), for the measured carrier concentrations (**Figure 4e** in the main text) and carrier mobilities (**Figure 4f** in the main text) of T_d-$Mo_{0.29}W_{0.72}Te_{1.99}$ and T_d- & $2H$-$Mo_{0.32}W_{0.67}Te_{2.01}$ present apparent differences in these two CVD-synthesized structures with different crystal phases. As described on **Figure 4a-d** in the main text, while the T_d-$Mo_{0.29}W_{0.72}Te_{1.99}$-FET exhibits semi-metallic behavior without an apparent gating effect, the T_d- & $2H$-$Mo_{0.32}W_{0.67}Te_{2.01}$-FET possesses p-type semiconducting characteristic and supports the existence of the semiconductor crystal with the $2H$ phase. Notably, the resistivity $(1.1 \pm 0.3) \times 10^{-4}$ Ω cm in T_d-$Mo_{0.29}W_{0.72}Te_{1.99}$-FET is much smaller than that $(1.9 \pm 0.5) \times 10^{-3}$ Ω cm of T_d- & $2H$-$Mo_{0.32}W_{0.67}Te_{2.01}$-FET, emphasizing the faster electrical transport in the semi-metallic T_d-$Mo_{0.29}W_{0.72}Te_{1.99}$.

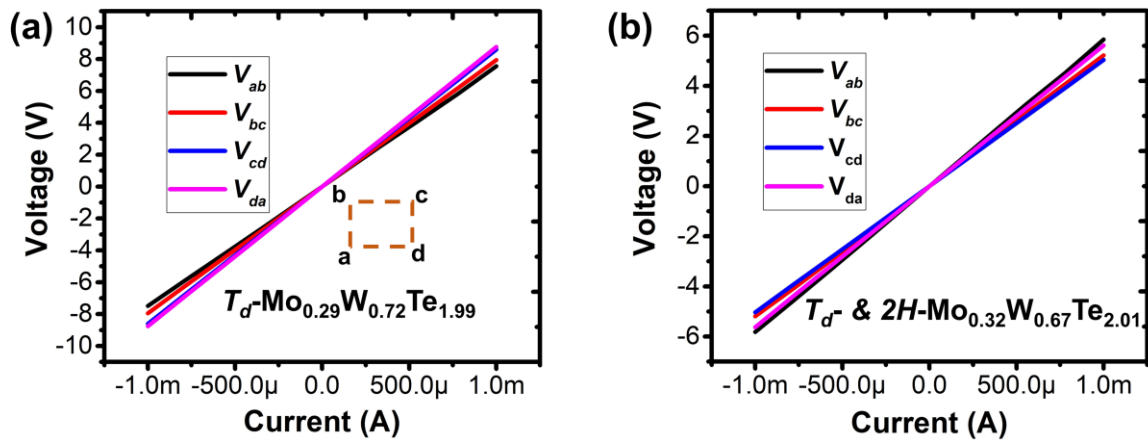**Figure S4.** In four-probe Hall effect measurements, the devices fabricated with (a) T_d-Mo$_{0.29}$W$_{0.72}$Te$_{1.99}$ and (b) T_d- & $2H$-Mo$_{0.32}$W$_{0.67}$Te$_{2.01}$ show ohmic contacts in the measured I-V curves.

Section S5. Electron Microscope Image and Elemental Mapping

Scanning electron microscopy (SEM) measurements were employed to characterize the morphologies of the CVD-synthesized $Mo_xW_{1-x}Te_2$ nanosheets and the sputtered Pt on CC substrates. **Figures S5a–d** display the SEM images of T_d- & $2H$-$Mo_{0.32}W_{0.67}Te_{2.01}$/CC, T_d-$Mo_{0.29}W_{0.72}Te_{1.99}$/CC, Pt/CC, and bare CC, respectively. While the insets of (**a–c**) present the elemental mappings by energy dispersive spectroscopy (EDS), the inset of (**d**) shows the enlarged view of the bare CC surface.
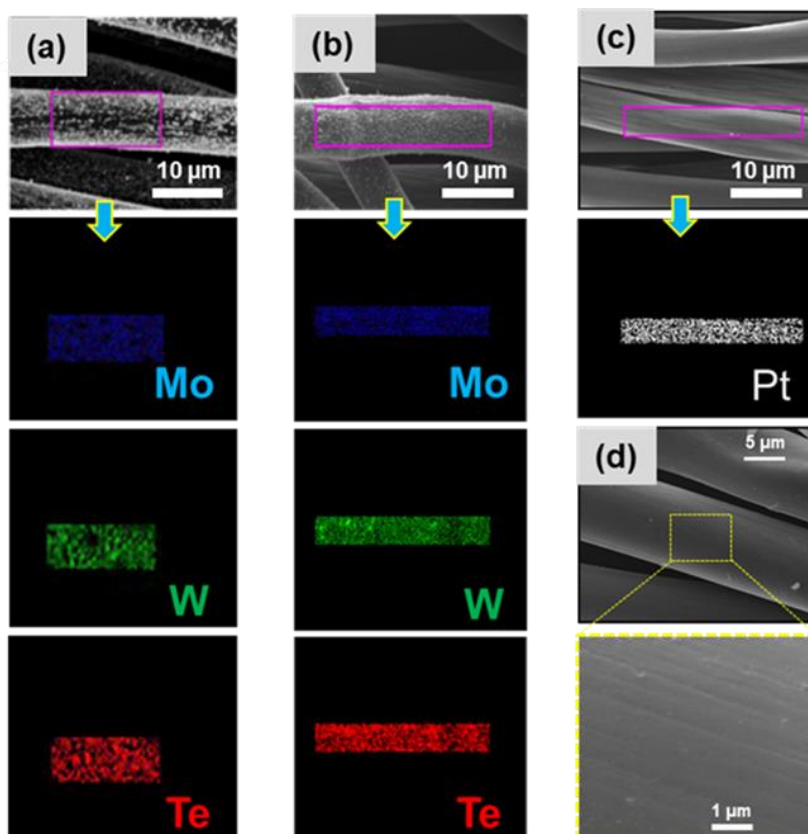

Figure S5. SEM images and elemental mappings on the selected area (demarcated by the purple frame lines) of (a) T_d- & $2H$-$Mo_{0.32}W_{0.67}Te_{2.01}$/CC, (b) T_d-$Mo_{0.29}W_{0.72}Te_{1.99}$/CC, (c) Pt/CC, and (d) bare CC. The insets of (a)–(c) show the EDS mappings of elemental distributions; the inset of (d) presents the enlarged view of the bare CC surface.

Section S6. Stability of a $Mo_xW_{1-x}Te_2$ Counter Electrode in the I^-/I_3^- Electrolyte

In **Figure S6,** the stabilities of the as-synthesized $Mo_xW_{1-x}Te_2$/CC and a standard Pt/CC, to be used as counter electrodes (CEs), were examined by cyclic voltammetry (CV) conducted in a three-electrode system. Over 200-cycle CV measurements, both T_d-$Mo_{0.29}W_{0.72}Te_{1.99}$/CC and T_d- & $2H$-$Mo_{0.32}W_{0.67}Te_{2.01}$/CC were found more stable than a standard Pt/CC. The J_{PC} values as a function of the measured cycle number are summarized in **Figure S6d**, where the abilities of CEs to reduce I_3^- into I^- are clearly indicated and T_d-$Mo_{0.29}W_{0.72}Te_{1.99}$/CC was found to hold the highest cathodic current density over T_d- & $2H$-$Mo_{0.32}W_{0.67}Te_{2.01}$/CC and Pt/CC.
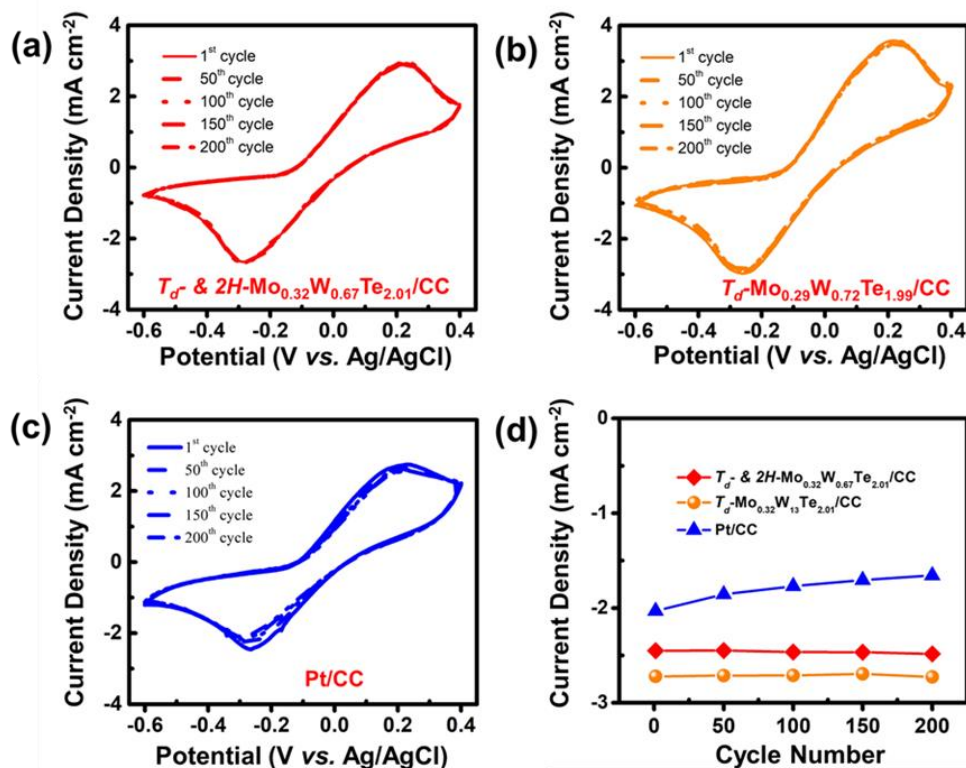
Figure S6. The stability of (a) T_d- & $2H$-$Mo_{0.32}W_{0.67}Te_{2.01}$/CC, (b) T_d-$Mo_{0.29}W_{0.72}Te_{1.99}$/CC, and (c) Pt/CC used as CEs were tested by 200-cycle CV measurements. The J_{PC} values as a function of the measured cycle number are summarized in (d). These measurements were carried out in a three-electrode electrochemical system.

Section S7. Materials

Lithium iodide (LiI, synthetic grade) and iodine (I_2, synthetic grade) were obtained from Merck. Acetone (99+ %), Tert-butyl alcohol (tBA, 96 %), guanidine thiocyanate (GuSCN, 99+ %), and 4-tert-butylpyridine (TBP, 96 %) were bought from Acros. Titanium (IV) tetraisopropoxide (TTIP, >98 %), lithium perchlorate ($LiClO_4$, ≥98.0 %), ethanol (EtOH, absolute), isopropyl alcohol (IPA, 99.5 %), sulfuric acid (H_2SO_4, 95–97 %), and 2-methoxyethanol (99.95 %) were received from Sigma-Aldrich. Acetonitrile (ACN, 99.99 %) was procured from J. T. Baker. 1,2-dimethyl-3-propylimidazolium iodide (DMPII) and cis-diisothiocyanato-bis(2,2'-bipyridyl-4,4'-dicarboxylato) ruthenium (II) bis(tetra-butylammonium) (N719 dye) were purchased from Solaronix, Switzerland. Carbon cloth (CC, W0S1002, thickness: 0.36 mm, basic weight: 120 g cm^{-2}, sheet resistance: 0.63 Ω sq.$^{-1}$) was purchased from CeTech, Taiwan.

References

[S1]   L. Zhou, K. Xu, A. Zubair, A. D. Liao, W. Fang, F. Ouyang, Y. H. Lee, K. Ueno, R. Saito, T. Palacios, J. Kong, M. S. Dresselhaus, *J. Am. Chem. Soci.* **2015**, 137, 11892.

[S2]   J. C. Park, S. J. Yun, H. Kim, J.-H. Park, S. H. Chae, S.-J. An, J.-G. Kim, S. M. Kim, K. K. Kim, Y. H. Lee, *ACS Nano* **2015**, 9, 6548.

[S3]   a) J. Beck, *Chem. Ber.* **1995**, 128, 23; b) A. F. H. Nils Wiberg , Egon Wiberg, *Acad. Press* **2001**, 588.

[S4]   a) E. L. a. W.-D. Schubert, *Kluwer Acad. Plen. Publ.* **1998**, 160; b) J. Tillack, *Inorg. Synth.* **1973**, 14, 109; c) V. C. Gibson, Kee, T. P., Shaw, A., *Polyhedron* **1988**, 7,, 579.

[S5]   Y. Gong, Z. Lin, G. Ye, G. Shi, S. Feng, Y. Lei, A. L. Elías, N. Perea-Lopez, R. Vajtai, H. Terrones, Z. Liu, M. Terrones, P. M. Ajayan, *ACS Nano* **2015**, 9, 11658.

[S6]   J. Zhou, F. Liu, J. Lin, X. Huang, J. Xia, B. Zhang, Q. Zeng, H. Wang, C. Zhu, L. Niu, X. Wang, W. Fu, P. Yu, T. R. Chang, C. H. Hsu, D. Wu, H. T. Jeng, Y. Huang, H. Lin, Z. Shen, C. Yang, L. Lu, K. Suenaga, W. Zhou, S. T. Pantelides, G. Liu, Z. Liu, *Adv. Mater* **2017**, 29.

[S7]   a) R. B. Sean M Oliver, Sergiy Krylyuk, Irina Kalish, Arunima K Singh, Alina Bruma, Francesca Tavazza, Jaydeep Joshi, Iris R Stone, Stephan J Stranick, Albert V Davydov and Patrick M Vora, *2D Mater.* **2017**, 4, 045008; b) D. Rhodes, D. A. Chenet, B. E. Janicek, C. Nyby, Y. Lin, W. Jin, D. Edelberg, E. Mannebach, N. Finney, A. Antony, T. Schiros, T. Klarr, A. Mazzoni, M. Chin, Y. c. Chiu, W. Zheng, Q. R. Zhang, F. Ernst, J. I. Dadap, X. Tong, J. Ma, R. Lou, S. Wang, T. Qian, H. Ding, R. M. Osgood, D. W. Paley, A. M. Lindenberg, P. Y. Huang, A. N. Pasupathy, M. Dubey, J. Hone, L. Balicas, *Nano Lett.* **2017**, 17, 1616.

[S8]   S. Cho, S. Kim, J. H. Kim, J. Zhao, J. Seok, D. H. Keum, J. Baik, D.-H. Choe, K. J. Chang, K. Suenaga, S. W. Kim, Y. H. Lee, H. Yang, *Science* **2015**, 349, 625.

[S9]   D. H. Keum, S. Cho, J. H. Kim, D.-H. Choe, H.-J. Sung, M. Kan, H. Kang, J.-Y. Hwang, S. W. Kim, H. Yang, K. J. Chang, Y. H. Lee, *Nat. Phys.* **2015**, 11, 482.